

G.A. Wallace  
EDB1

**CFD MODELING OF TURBULENT FLOWS AROUND THE SSME  
MAIN INJECTOR ASSEMBLY USING POROSITY FORMULATION**

Contract No. NAS8-38871  
Final Report

Prepared for:

National Aeronautics & Space Administration  
George C. Marshall Space Flight Center  
Marshall Space Flight Center, AL 35812

By

Gary C. Cheng  
Y.S. Chen  
Richard C. Farmer

SECA, Inc.  
3313 Bob Wallace Ave., Suite 202  
Huntsville, AL 35805

May, 1992

(NASA-CR-184359) CFD MODELING OF  
TURBULENT FLOWS AROUND THE SSME  
MAIN INJECTOR ASSEMBLY USING  
POROSITY FORMULATION Final Report  
(SECA) 57 p

N93-11171

Unclass

G3/34 0117770

482932 588

# **CFD MODELING OF TURBULENT FLOWS AROUND THE SSME MAIN INJECTOR ASSEMBLY USING POROSITY FORMULATION**

**Contract No. NAS8-38871  
Final Report**

**Prepared for:**

**National Aeronautics & Space Administration  
George C. Marshall Space Flight Center  
Marshall Space Flight Center, AL 35812**

**By**


**Gary C. Cheng  
Y.S. Chen  
Richard C. Farmer**

**SECA, Inc.  
3313 Bob Wallace Ave., Suite 202  
Huntsville, AL 35805**

**May, 1992**

## ABSTRACT

ORIGINAL CONTAINS  
COLOR ILLUSTRATIONS



Hot gas turbulent flow distribution around the main injector assembly of the Space Shuttle Main Engine (SSME) and LOX flow distribution through the LOX posts have a great effect on the combustion phenomena inside the main combustion chamber. In order to design a CFD model to be an effective engineering analysis tool with good computational turn-around time (especially for 3-D flow problems) and still maintain good accuracy in describing the flow features, the concept of porosity was employed to describe the effects of blockage and drag force due to the presence of the LOX posts in the turbulent flow field around the main injector assembly of the SSME. ~~2-D~~ <sup>2-D</sup> numerical studies were conducted to identify the drag coefficients of the flows, both through tube banks and around the shielded posts, over a wide range of Reynolds numbers. Empirical, analytical expressions of the drag coefficient as a function of local flow Reynolds number were then deduced. The porosity model was applied to the turbulent flow around the main injector assembly of the SSME, and analyses were performed. The 3-D CFD analysis was divided into three parts; LOX dome, hot gas injector assembly, and hydrogen cavity. The numerical results indicate that the mixture ratio at the downstream of injector face was close to stoichiometric around baffle elements.

# TABLE OF CONTENTS

<b>ABSTRACT</b> .....	i
<b>1.0 INTRODUCTION</b> .....	1
1.1 THE NATURE OF THE PROBLEM .....	1
1.2 OBJECTIVE .....	1
<b>2.0 CFD METHODOLOGY</b> .....	3
2.1 GOVERNING EQUATIONS .....	4
2.2 NUMERICAL ALGORITHM .....	5
<b>3.0 PROPOSED POROSITY MODEL</b> .....	9
3.1 2-D TUBE BANK FLOWS STUDIES .....	10
3.2 TURBULENT FLOW AROUND SHIELDED POST ELEMENTS ...	13
3.3 LOSS COEFFICIENT MODEL .....	17
<b>4.0 NUMERICAL RESULTS</b> .....	19
4.1 LOX DOME .....	19
4.2 HOT GAS INJECTOR ASSEMBLY .....	25
4.3 HYDROGEN CAVITY .....	38
4.4 MAIN INJECTOR ASSEMBLY .....	44
<b>5.0 CONCLUSIONS AND RECOMMENDATIONS</b> .....	50
<b>REFERENCES</b> .....	51



## **1.0 INTRODUCTION**

### **1.1 THE NATURE OF THE PROBLEM**

Fluid flow and heat transfer in the main injector assembly of the Space Shuttle Main Engine (SSME) are complex phenomena. The basic understanding these phenomena is essential to achieving optimum performance during normal operating conditions and maintaining structural integrity during off-design operations. The mixture ratio and mass flow rate distributions of the SSME main injector assembly will greatly affect 1) engine performance, and 2) heat loads of the combustion chamber; especially, the later effect is directly linked to the durability of the engine. Historically, the SSME has been suffering burn out of the LOX post baffle elements and erosion of the combustion chamber during firings. In order to investigate possible causes of such damage, understanding the flow field at main injector exit is essential. The geometry of the SSME main injector assembly is extremely complex, and its flow field is three-dimensional and turbulent. Conventional three-dimensional computational fluid dynamic (CFD) models are not practical to describe the necessary geometric detail of the SSME main injector assembly. The flow description was simplified by utilizing the concept of porosity to provide an effective engineering design tool for this system.

### **1.2 OBJECTIVE**

The objective of this study was to develop a practical CFD simulation of the main injector assembly. The geometric complexity caused by the use of hundreds of individual LOX-post elements was reduced to a manageable computation by using non-isotropic porosity and

distributed resistance models. LOX-post arrays, shielded LOX-posts, and flows through porous injector plates were characterized with blockage and resistance models. A non-isotropic porosity model was incorporated into an existing Navier-Stokes flow solver (FDNS). Volume and surface porosity parameters, which are based on the configurations of local lox-post clustering, were introduced into the governing equations. Accuracy and robustness of the proposed model was demonstrated through data comparisons with benchmark test data and with detailed CFD solutions. Application of the postulated model to the turbulent flow within the main injector assembly of the SSME was made. This design tool predicts the local O/F distribution of the flow entering the main combustion chamber.

## 2.0 CFD METHODOLOGY

The turbulent flow around the LOX post assembly is similar to the flow through a tube bank ensemble. There are basically three methods available in the literature (Ref. 1) to analyze the fluid dynamics and heat transfer characteristics of flow-cylinder assemblies with various configurations. These methods are: 1) sub-channel analysis; 2) porosity and distributed resistance approach (Ref. 2); and 3) benchmark detail rod-bundle fluid/thermal dynamics analysis using boundary fitted coordinate (BFC) system (Refs. 3,4). The first method is a simplified approach of the second method. Although the last method of analysis can provide the most detailed computational results, the mesh size required to resolve the geometrical complexity of the entire main injector assembly prohibits its use as an effective engineering design/analysis tool. One solution for this problem is the use of porosity modeling in the CFD analysis which will provide much better computer turn-around time. Validity of the approximations employed in the porosity model can be verified by comparing with the detailed CFD/BFC solutions for geometrically simplified test cases. A non-isotropic porosity model was developed and validated by comparing to the 2-D tube bank flows over a wide range of Reynolds numbers. The mass flow rate through the post element and the porous plate was also calculated by using the distributed resistance model. The non-isotropic porosity and the distributed resistance models were incorporated into the Navier-Stokes flow solver (FDNS).

## 2.1 GOVERNING EQUATIONS

The FDNS code (Refs. 5-7) is a time-accurate pressure-based predictor-corrector flow solver. Various turbulence models, such as standard k- $\epsilon$  mode, extended k- $\epsilon$  model (Ref. 8), low Reynolds number k- $\epsilon$  model, along with different compressibility corrections, have also been incorporated into the code. The FDNS code solves the following form of the conservation equations, including the continuity equation, the Navier-Stokes equations, the energy equation, and two-equation turbulence models, in curvilinear coordinates:

$$\frac{1}{J} \frac{\partial \rho q}{\partial t} = - \frac{\partial F_i}{\partial \xi_i} + S_q = R_q = \text{Residual} \quad (1)$$

where  $q$  stands for dependent variables (i.e. unity, the velocity vectors, temperature, turbulence quantities, and mass fractions of chemical species), and the numerical flux,  $F$ , is the sum of a convective flux,  $F_c$ , and a viscous flux,  $F_v$ , i.e.

$$F = F_c + F_v, \quad F_c = \rho U_i q, \quad F_v = -\mu_{\text{eff}} G_{ij} \frac{\partial q}{\partial \xi_i} \quad (2)$$

where  $J$ ,  $U_i$  and  $G_{ij}$  represent the Jacobian of the coordinate transformation, transformed velocities, and diffusion metrics, respectively. They are written as

$$J = \frac{\partial(\xi, \eta, \zeta)}{\partial(x, y, z)}, \quad U_i = \frac{u_i}{J} \frac{\partial \xi_i}{\partial x_j}, \quad G_{ij} = \frac{1}{J} \frac{\partial \xi_i}{\partial x_k} \frac{\partial \xi_j}{\partial x_k} \quad (3)$$

$\mu_{\text{eff}} = (\mu_t + \mu_r)/\sigma_q$  is the effective viscosity when the turbulent eddy viscosity concept is employed to model the turbulent flows.  $\mu_t = \rho C_\mu k^2/\epsilon$ , is the turbulence eddy viscosity and  $C_\mu$  and  $\sigma_q$  denote turbulence modeling constants, and  $k$  and  $\epsilon$  are the turbulence kinetic energy and

its dissipation rate; while  $\mu_f$  is the fluid viscosity. Source terms  $S_q$  for the continuity, momentum, energy and species equations are given by

$$S_q = \frac{1}{J} \left\{ \begin{array}{c} 0 \\ -\frac{\partial p}{\partial x} + \nabla \left[ \mu_{eff} \frac{\partial u_j}{\partial x} \right] - \frac{2}{3} \frac{\partial \mu_{eff}}{\partial x} \nabla u_j \\ -\frac{\partial p}{\partial y} + \nabla \left[ \mu_{eff} \frac{\partial u_j}{\partial y} \right] - \frac{2}{3} \frac{\partial \mu_{eff}}{\partial y} \nabla u_j \\ -\frac{\partial p}{\partial z} + \nabla \left[ \mu_{eff} \frac{\partial u_j}{\partial z} \right] - \frac{2}{3} \frac{\partial \mu_{eff}}{\partial z} \nabla u_j \\ \frac{\partial p}{\partial t} + \nabla \left[ (\sigma_T - 1) \mu_{eff} \nabla \left( \frac{V^2}{2} \right) \right] \\ \rho (P_r - \epsilon) \\ \frac{\rho \epsilon}{k} (C_1 P_r - C_2 \epsilon) \\ \omega_n, \quad n = 1, \dots, N \end{array} \right\} \quad (4)$$

where  $p$  and  $u_j$  are the static pressure and velocity vectors,  $V^2 = \sum u_j^2$ ,  $P_r$  is the turbulence kinetic energy production rate,  $\omega_n$  is the species production rate, where  $C_1$ ,  $C_2$ , and  $\sigma_T$  are turbulence modeling constants. The equation of state for an ideal gas or a real gas is used to close the above system of equations. These equations were solved with the pressure-based FDNS solver, which is discussed in detail in Refs. 5 & 6.

## 2.2 NUMERICAL ALGORITHM

A pressure based solution method is employed in FDNS so that a wide range of flow speeds can be analyzed with the same code. For high speed flow cases, a hyperbolic pressure

correction equation is retained by perturbing the density in the mass conservation equation. This provides a smooth transition from low speed to high speed flows. For time accuracy, a time-centered, time-marching procedure with a multiple pressure corrector algorithm is employed. This method provides numerical efficiency for time-dependent flow problems.

To solve the system of nonlinear coupled partial differential equations, finite difference approximations are used to establish a system of linearized algebraic equations. A relaxation solution procedure is then employed to couple the equations. First, equation (2) is discretized in time with a time-centered (Crank-Nicholson) scheme. That is,

$$\frac{1}{J\Delta t} [(\rho q)^{n+1} - (\rho q)^n] = \frac{R_q^{n+1} + R_q^n}{2} \quad (5)$$

where the superscripts  $n$  and  $n+1$  denote the current time level and the next time level, respectively. If a sub-iteration procedure, designated by a superscript  $k$ , within a time step is applied, the following linearization is incorporated.

$$(\rho q)^{n+1} = (\rho q)^k + \rho^n \Delta q^k \quad (6)$$

$$R_q^{n+1} = \left( \frac{\partial R_q}{\partial q} \right)^k \Delta q^k + R_q^k \quad (7)$$

With the above linearization, the final form of the time-marching scheme is written as

$$\left[ \left( \frac{\rho}{J\Delta t} \right)^n - \left( \frac{\partial R_q}{\partial q} \right)^k \right] \Delta q^k = - \frac{1}{J\Delta t} [(\rho q)^k - (\rho q)^n] + \frac{R_q^k + R_q^n}{2} \quad (8)$$

The solution at time level  $n+1$  is then updated by

$$q^{n+1} = q^{k+1} = q^k + \Delta q^k \quad (9)$$

when  $k = 1$  is selected, a non-iterative time-marching scheme is used. As reported in Ref. 6, the non-iterative option with a multi-corrector solution method provides time accurate solutions for transient flow problems. This multi-corrector procedure is described briefly below.

A simplified momentum equation is combined with the continuity equation to form a pressure correction equation. This pressure correction equation exhibits elliptical behavior for low speed flow and becomes continuously more hyperbolic as flow speed increases. The simplified momentum equation can be written as

$$\frac{\partial \rho u_i}{\partial t} \approx -\nabla p', \quad \text{or} \quad u_i \approx -\frac{\Delta t}{\rho} \nabla p' \quad (10)$$

where the superscript  $'$  denotes perturbations. The velocity and density fields in the continuity equation are then perturbed to form a correction equation. That is

$$\nabla(\rho u_i)^{n+1} = \nabla[(\rho^n + \rho')(u_i^n + U_i')] \quad (11)$$

By neglecting the  $\rho' u_i'$  terms, the following equation results.

$$\nabla(u_i \rho') + \nabla(\rho u_i') = -\nabla(\rho u_i)^n \quad (12)$$

Equation (12) has the form of a transport equation with convection and diffusion terms. Upwind treatment can be used to model the left hand side of equation (12). A dissipation term is also added to the right hand side of equation (12) to provide smooth shock solutions. Using the solution of equation (12), the pressure and velocity fields are updated and the density field is then

updated by using the equation of state. This corrector procedure is repeated several time (usually 4 times are sufficient) before marching to the next time step. This procedure insures that the mass conservation condition is satisfied for each time step. This represents the multi-corrector solution procedure. This method requires one predictor step and less than four corrector steps to provide numerical efficiency for transient flow computations.



### 3.0 PROPOSED POROSITY MODEL

The conventional porosity models assume the use of orthogonal coordinates and geometrically similar control volumes (Refs. 1 & 2). In the proposed approach, the general boundary fitted coordinate systems were incorporated in the formulation. Two new parameters, volume porosity ( $\gamma_v$ , defined as the ratio of the volume occupied by the fluid to the total volume) and surface porosity ( $\gamma_i$ , defined as the ratio of the surface area in the  $i$ -direction available for flow to the corresponding total surface area in the same direction), were introduced into the flow governing equations. For the proposed porosity model, equation (1) was rewritten as

$$\frac{\gamma_v}{J} \frac{\partial \rho q}{\partial t} = - \frac{\partial \gamma_i F_i}{\partial \xi_i} + \gamma_v S_q = R_q = \text{Residual} \quad (13)$$

A distributed drag force  $D$  and a heat flux  $H$  source term were also added to the right hand side of the momentum equation and the energy equation, respectively, to simulate the effects of resistance and heat transfer due to the presence of the LOX posts in the flow field. These drag force and heat flux terms were modeled based on geometric parameters and the averaged velocity around a local LOX post. Since the drag force  $D$  is defined as

$$D = 0.5 \rho u^2 C_D \quad (14)$$

where  $\rho$ ,  $u$ , and  $C_D$  are local flow density, local total velocity, and local drag coefficient, respectively, we can compute the distributed drag force by evaluating these three parameters. 2-D tube bank flow studies were investigated to verify the drag coefficients for the flow around the LOX posts assembly. Moreover, the 13th row posts are shielded in pairs, where on the shield

surface there are several holes distributed between each pair of posts. Additional CFD validation studies were needed to identify the drag coefficients for the flow around shielded elements.

### 3.1 2-D TUBE BANK FLOW STUDIES

The CFD investigation of the flow through the tube bank configuration was conducted for various Reynolds numbers ( $Re$ ), such as 20,  $10^5$ ,  $10^6$ , and  $10^7$ . The flow fields of the  $Re=20$  case and the  $Re=10^6$  case are demonstrated in Figures 1 & 2, and the computed pressure distribution along the cylinders with these four Reynolds numbers are plotted as shown in Figures 3-6.

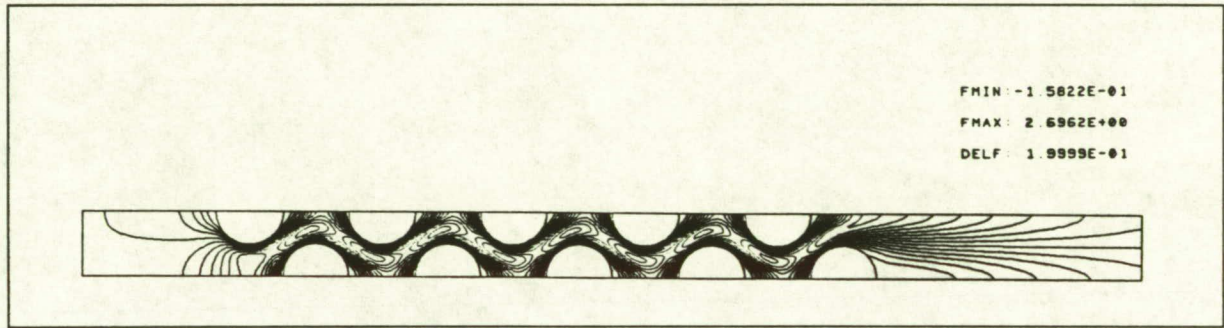


Figure 1 Streamline Velocity ( $u$ ) contours for the Flow Past a 2-D Tube Bank with  $Re=20$

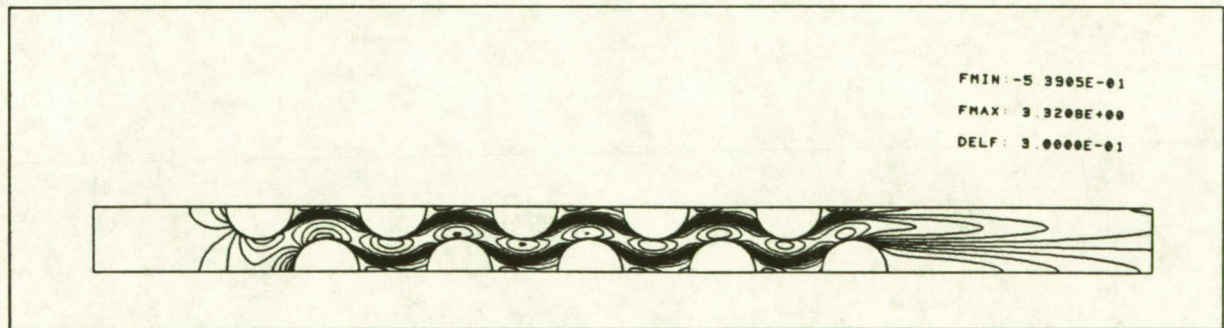


Figure 2 Streamline Velocity ( $u$ ) contours for the Flow Past a 2-D Tube Bank with  $Re=10^6$

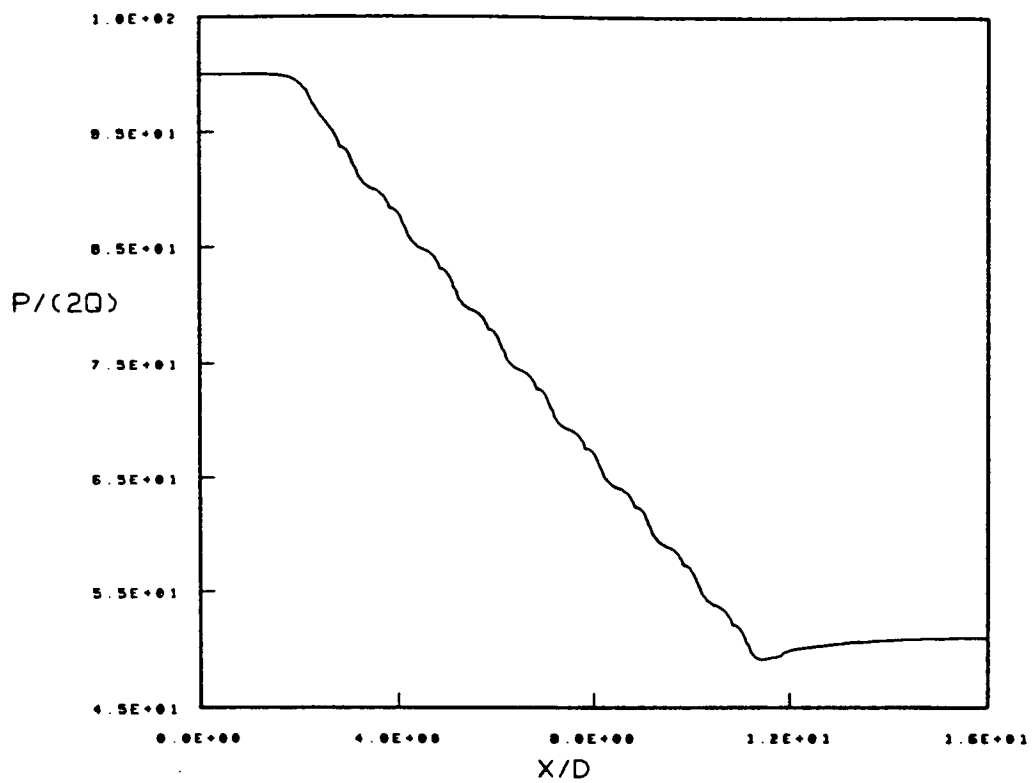


Figure 3 Static Pressure Distribution for the Flow Past a 2-D Tube Bank with  $Re=20$

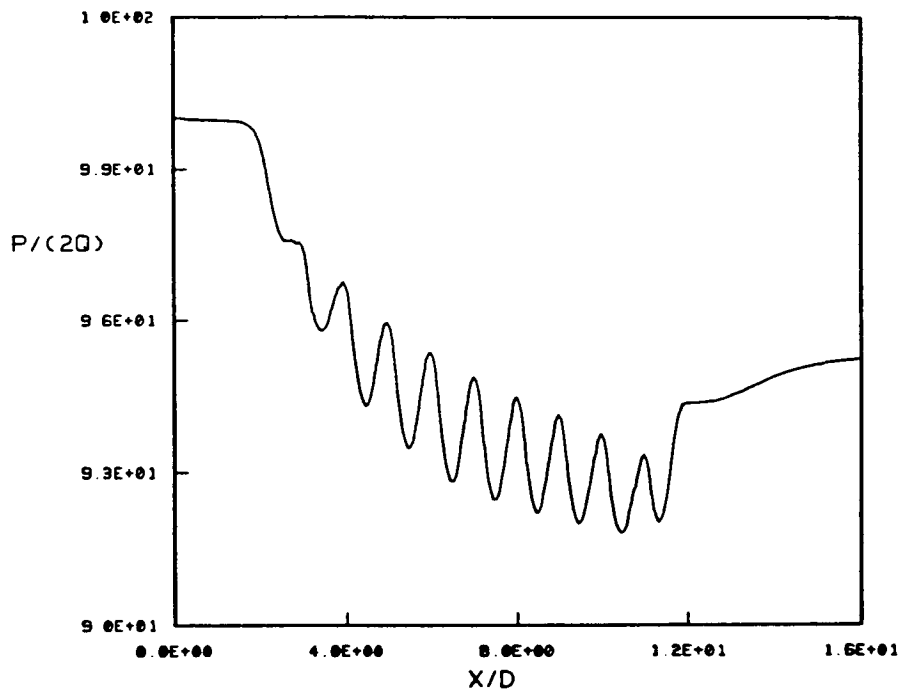


Figure 4 Static Pressure Distribution for the Flow Past a 2-D Tube Bank with  $Re=10^5$

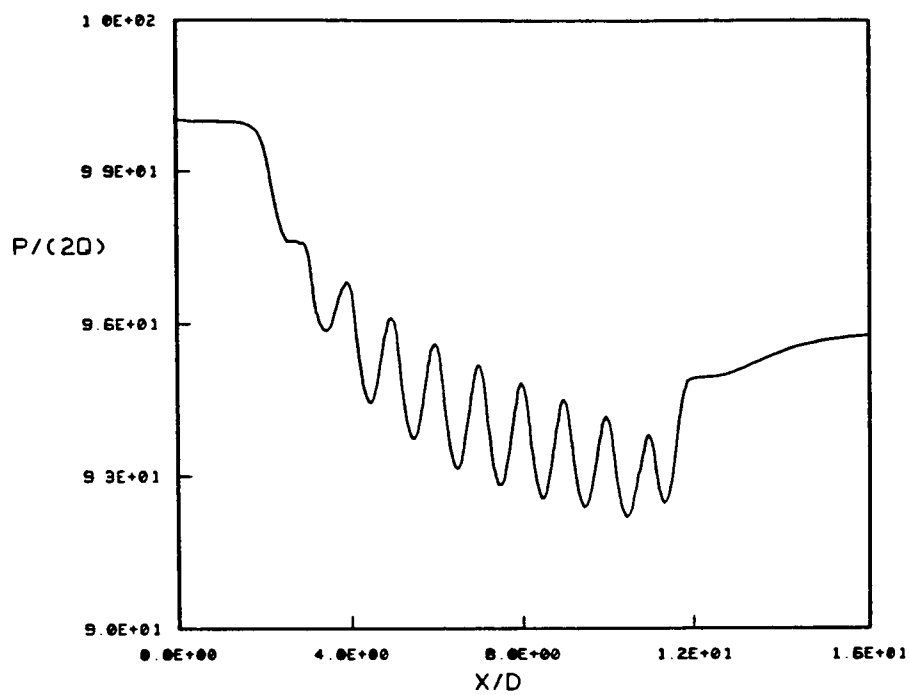


Figure 5 Static Pressure Distribution for the Flow Past a 2-D Tube Bank with  $Re=10^6$

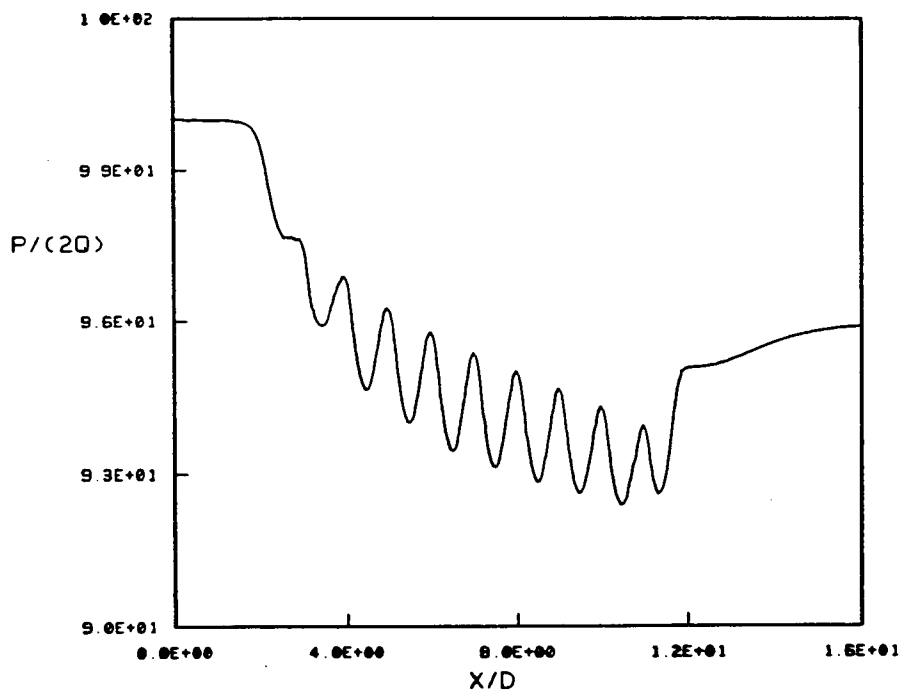


Figure 6 Static Pressure Distribution for the Flow Past a 2-D Tube Bank with  $Re=10^7$



Based on the CFD studies and a literature review (Refs. 9-14), a drag coefficient model for the tube bank flows is proposed as shown in Table 1. The proposed model was compared with the numerical results from previous benchmark cases and relatively good agreement has been achieved.

Table 1. The Drag Coefficient Model for Tube Bank Flow

	$C_d$
$Re < 4 \times 10^3$	$0.417 \text{ EXP}(4.932 \text{ Re}^{-0.296})$
$4 \times 10^3 < Re < 6 \times 10^4$	$0.647 - 0.5 \times 10^{-6} Re$
$6 \times 10^4 < Re < 10^6$	$0.618 + 0.491 \times 10^{-6} Re - 6.303 \times 10^{-12} Re^2$ $+ 10.694 \times 10^{-18} Re^3 - 5.2 \times 10^{-24} Re^4$
$Re > 10^6$	0.2735

### 3.2 TURBULENT FLOW AROUND SHIELDED POST ELEMENTS

In the hot gas injector region, the outer row (#13) is protected by shields to avoid damages caused by direct impingement on the LOX posts from the high speed gases. There are four types of shield, #039, #037, #025, and #023, where the configurations of shield-039 and shield-023 are sketched as shown in Figure 7. All the shields enclose two posts in one shield, except shield-025 which encloses three posts in one shield. The hole distribution on shield-025 is similar to that on shield-023, and there is only one shield-025 on row #13; hence shield-025

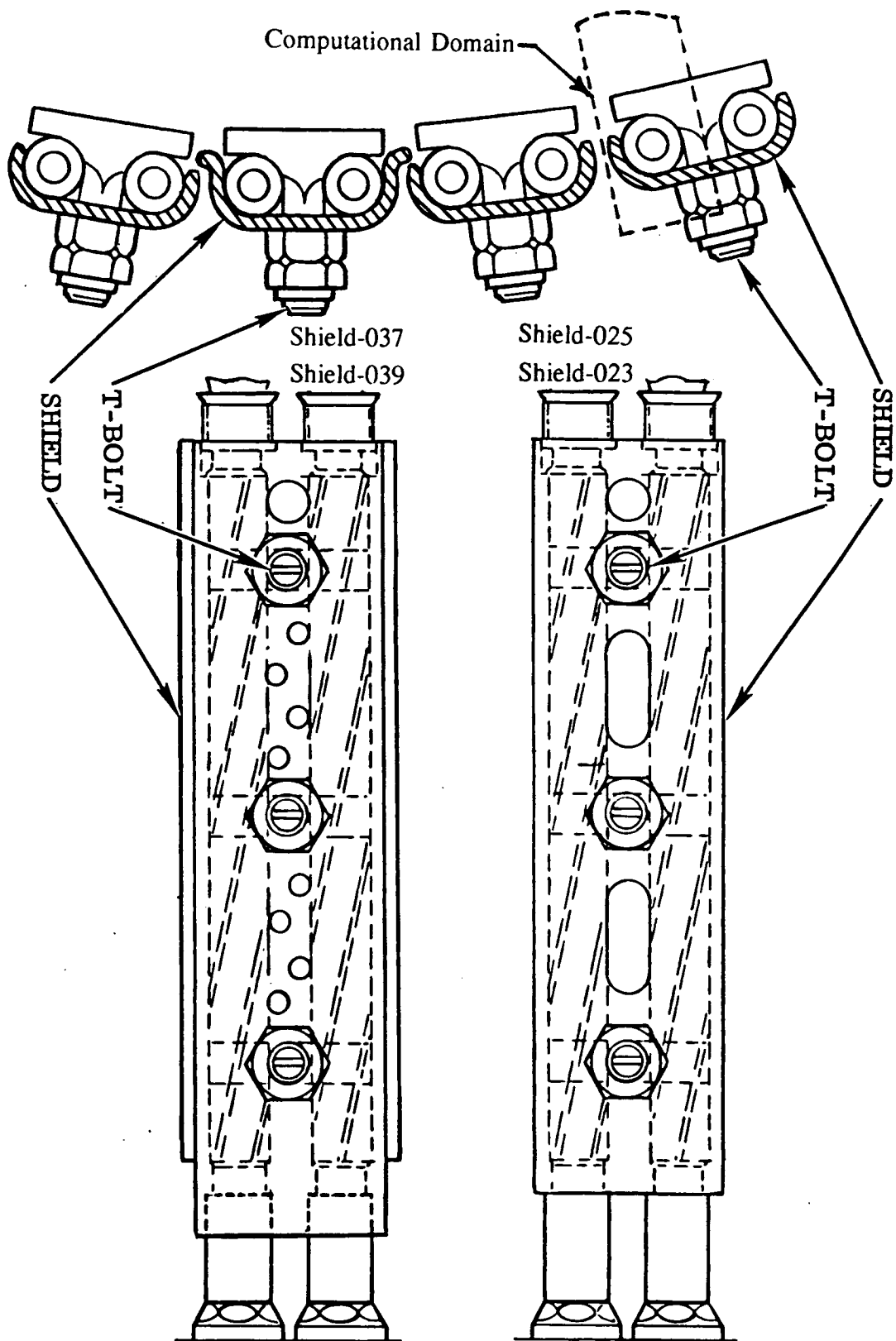


Figure 7 The Configuration of the Various Shielded Elements

was modeled the same as shield-023 in the numerical analysis. Shield-037 has the same type of hole distribution as shield-039, but shield-037 does not have the wing at the end of the shield. There are six #037 shields and five #039 shields, and they are installed in an alternating sequence and are located near the fuel side. In the proposed porosity, the drag coefficient for both shield-039 and shield-037 was assumed to be identical and was obtained from the numerical analysis of shield-037 geometry. Therefore, in this study all shields were considered to be of either the 023 or 037 type. CFD analyses were conducted for these two types of shields to obtain the porosity model for the flow through a shielded element.

Since the presence of the shield will greatly increase the drag force, numerical studies were performed to investigate the drag coefficient for the flow through the shielded elements with and without holes. Both 3-D and 2-D analyses were performed. Since the shielded elements are located on the outer row of the post assembly, the Reynolds number of the inlet flow to the shielded elements is relatively high and is around  $10^6$ . A symmetry boundary condition was specified at the centerline of the gap between posts to minimize the computational domain as indicated in Figure 7. The effect of the T-bolt as shown in Figure 7 was not taken into account in this study. An approximation for different types of holes on the shields was made to relax the requirement of using numerous grids to resolve these holes. The approximation was to treat the cross-section of various holes as rectangles with their width equal to the gap between each pair of posts. Therefore, the same drag coefficient model would be employed for various types of shields. The way to distinguish the difference between various types of shield is to identify the vertical locations of each hole and to use different porosity for different types of shields.

The numerical studies indicate that the drag coefficient does not change appreciably as the Reynolds number varies around  $10^6$ . The computed drag coefficient is close to 4 for the region with holes on the shield, and is close to 48 for the region without holes. The calculated flow fields for the flow through the shielded element with holes and without holes are exhibited in Figures 8a & 8b, respectively.

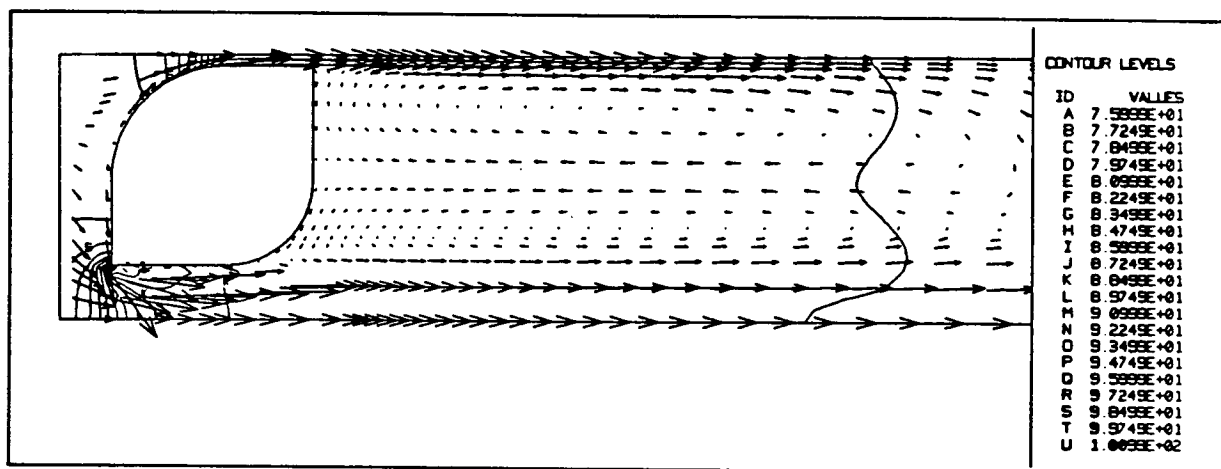


Figure 8a Pressure Contours and Velocity Vectors for the Flow Past a Shielded Element with Holes

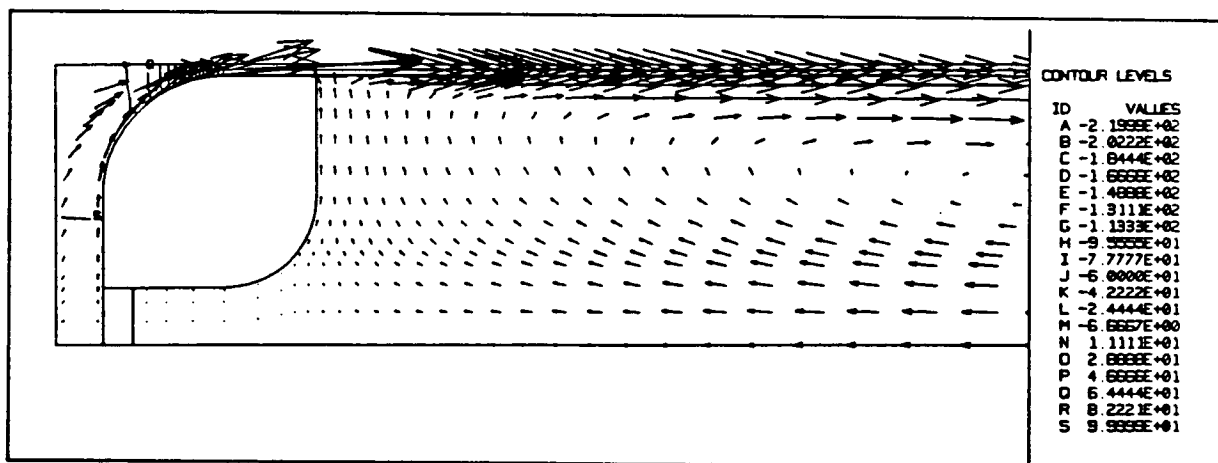


Figure 8b Pressure Contours and Velocity Vectors for the Flow Past a Shielded Element Without Holes



### 3.3 LOSS COEFFICIENT MODEL

In addition to the drag coefficient model for the flow through tube bank environment, a loss coefficient model is required to compute the mass flow rate for the flow through various porous media, such as an individual LOX post, porous plates, and boundary layer control (BLC) holes. To relate the mass flow rate and pressure drop across the porous media, the following loss coefficients ( $K$ ) are defined.

$$K = \frac{\rho \Delta p}{\dot{m}^2}, \quad \Delta p = p - p_{\text{chamber}}, \quad \text{or} \quad \Delta p = p - p_{\text{baffle}} \quad (15)$$

where  $\rho$ ,  $p$  are the density and static pressure at the exit plane, and  $\dot{m}$  is the mass flow rate through a porous medium. The value of the loss coefficient ( $K$ ) for each porous medium will be given later in the NUMERICAL RESULTS section. Therefore, the exit mass flow rate through each porous medium was computed based on the distributions of local loss coefficient and local exit pressure. In the numerical analysis, the area for each porous medium is different at each radial location; however, this is not true in the real geometry. Hence, in the computational domain, the area effect was excluded from the mass flow rate calculation. The assembly of the loss coefficients in the computational domain is then defined as

$$K' = \frac{\rho \Delta p}{\dot{M}^2}, \quad \text{i.e.} \quad \dot{M} = \sqrt{\frac{\rho \Delta p}{K'}} \quad (16)$$

where  $K'$  and  $\dot{M}$  are the global loss coefficient and mass flow rate for a type of porous medium, respectively. Hence, the local mass flow rate  $\dot{m}$  can be calculated as

$$\dot{m} = \dot{M} \frac{A_i}{A} = \sqrt{\frac{\rho \Delta p}{K'}} \frac{A_i}{A} \quad (17)$$

where  $A$  and  $A_i$  denote the global and local exit areas for the same type of porous medium, respectively. The value of the global loss coefficient ( $K'$ ) for each porous medium will also be reported later in the numerical results.

## 4.0 NUMERICAL RESULTS

The 3-D porosity/CFD analysis of the SSME main injector assembly was performed for the phase II+ power head geometry at the 104% power balance level. The entire configuration was divided into three components: 1) LOX dome, 2) hot gas injector assembly, and 3) hydrogen cavity. The overall mass flow rate distribution and mixture ratio distribution was calculated by superimposing the results from these three components. The numerical computation for these three components was conducted independently, except the calculated exit pressure of the hot gas injector assembly was employed as the back pressure for the secondary face plate in the hydrogen cavity region. The exit pressure to the combustion chamber  $p_{\text{chamber}}$  was assumed to be uniform and equal to 3135 psi. The exit pressure from baffle elements  $p_{\text{baffle}}$  was also assumed to be constant and have the value of 3084 psi.

### 4.1 LOX DOME

The LOX dome geometry was simulated as shown in Figure 9 with a 62 x 91 x 16 mesh system. The bleed pipes to the first three rows of the LOX posts were omitted and were replaced with the exit flow through the nose region. This simplification reduced the number of grid points required and required less detailed information for the bleed pipe geometry. The importance of the mass flow rate distribution for the first three rows of the LOX post was mitigated by the 1-D analytical result which indicates that the magnitude of the mass flow rate is relatively uniform among these three rows. The numerical analysis was conducted based on incompressible, adiabatic, turbulent flow with single species (liquid oxygen). The inlet flow conditions and loss

6R10

62x91x16

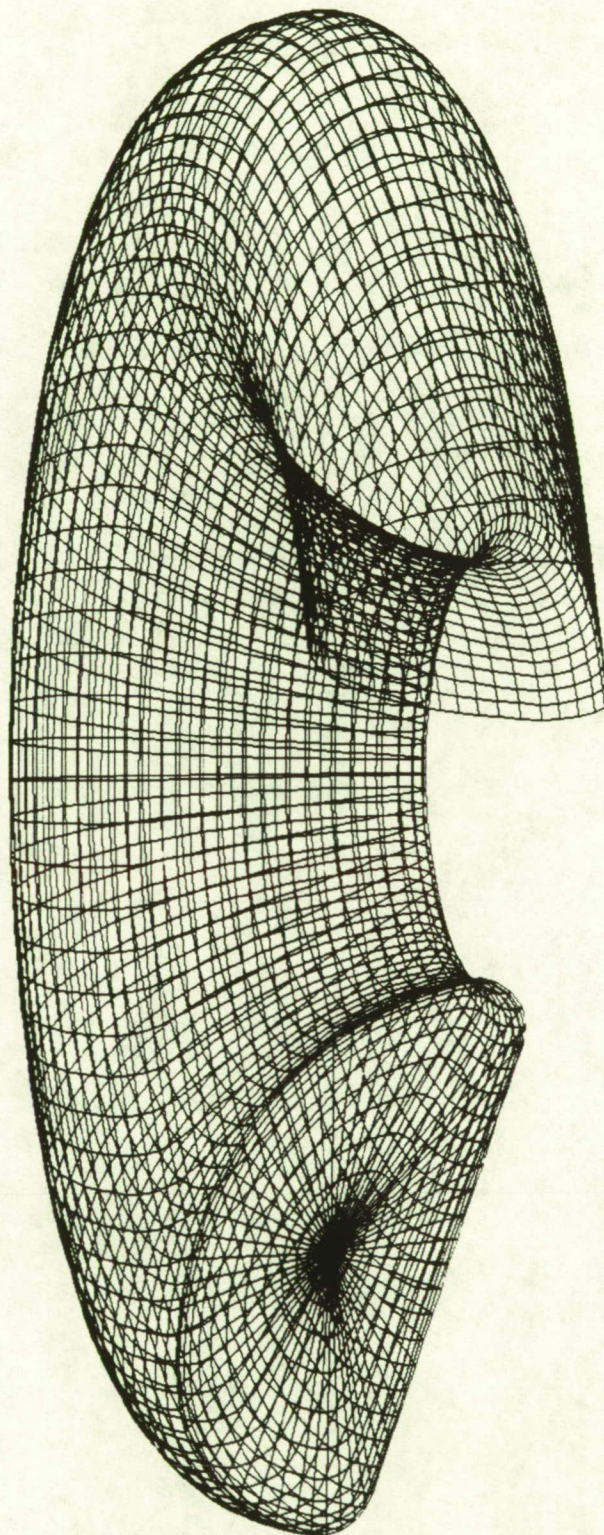


Figure 9 The Mesh System for the LOX Dome Geometry



coefficients are listed in Table 2 and 3, respectively. Uniform inlet velocity profiles were used because at the LOX tee exit no other information was available.

Table 2 Inlet Flow Conditions to the LOX Dome (104% RPL)

Static Pressure	Static Temperature	Reynolds Number	Mass Flow Rate
3670 psi	197 °R	$1.28 \times 10^8 \text{ ft}^{-1}$	826.7 lb/sec

Table 3 The Loss coefficient model for the LOX dome region (104% RPL)

	$\dot{m}$ (lb/sec)	$K$ (ft <sup>4</sup> )	$\dot{M}$ (lb/sec)	$K'$ (ft <sup>4</sup> )
Non-Baffle Elements	1.38	$9.62 \times 10^7$	665.105	$4.14 \times 10^2$
Baffle Elements	1.433	$9.78 \times 10^7$	105.65	$1.79 \times 10^4$
First Three Rows	1.332	$1.03 \times 10^8$	56.154	$5.81 \times 10^4$

Based on the above inlet flow conditions and the proposed loss coefficient model, a 3-D numerical computation was performed. Figure 10, top view of the velocity vector plot, exhibits the LOX flow around the LOX dome. The cross-sectional views of the four velocity vector planes in Figure 10 are plotted as shown in Figures 11a-11d. It is clearly shown that two recirculation zones occur in the plane with inlet flow, but a very smooth flow structure is formed



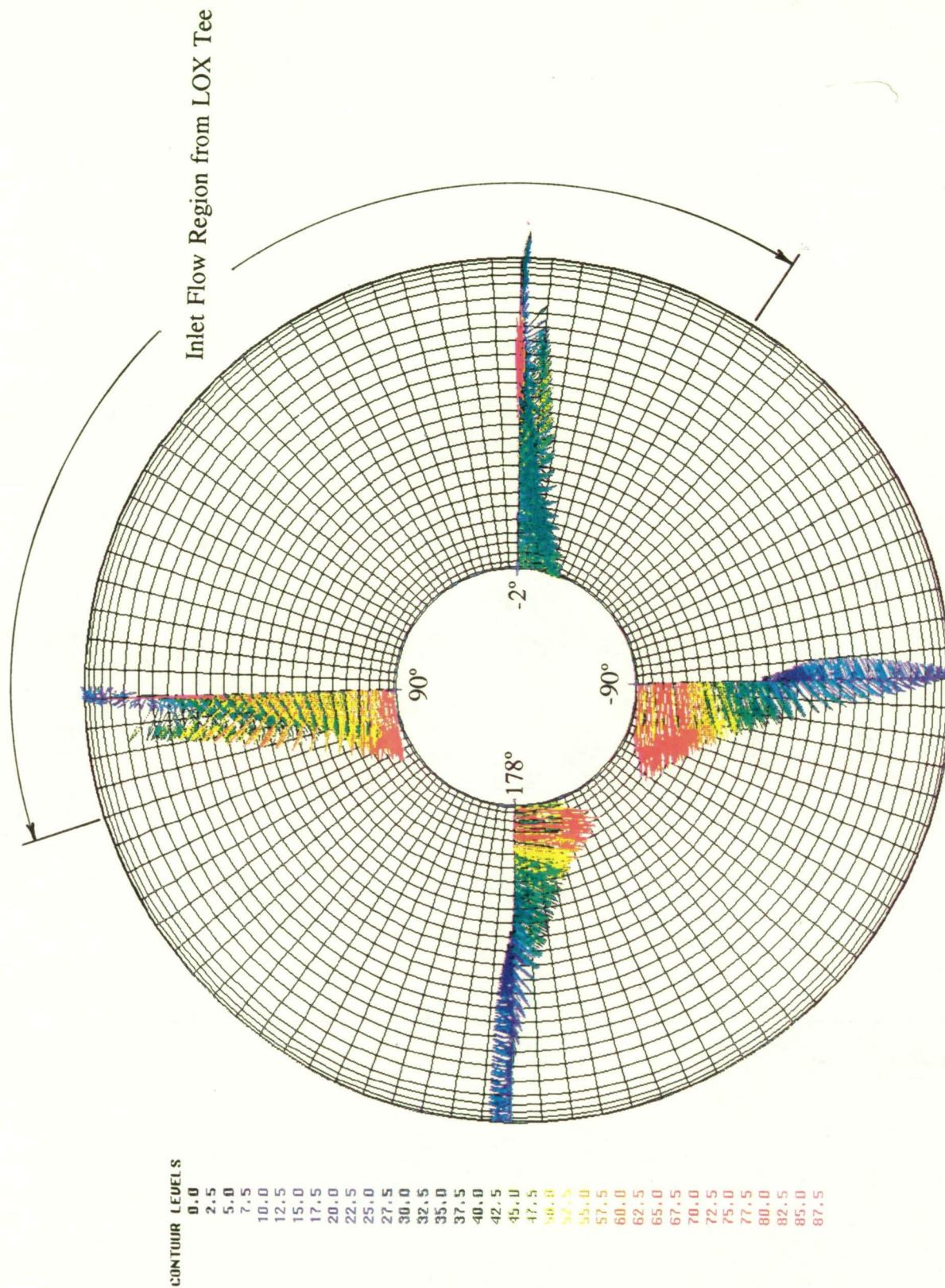


Figure 10 Top View of the Velocity Vectors in the LOX Dome, ft/sec (Fuel Side on the Bottom)



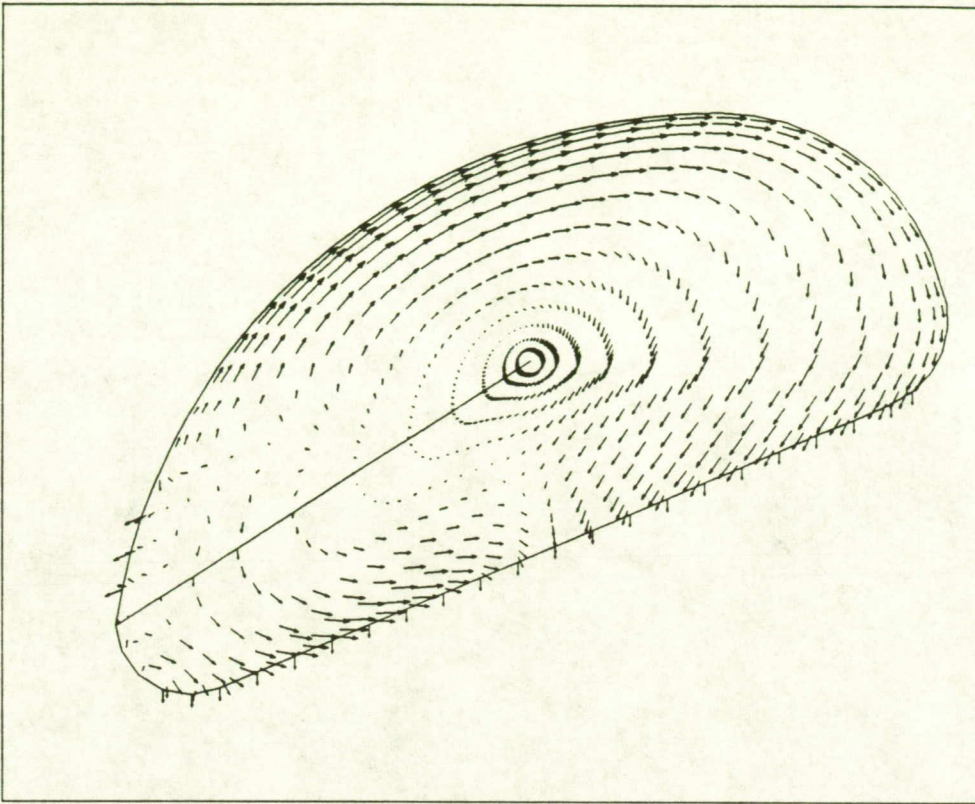


Figure 11a Velocity Vectors in the LOX Dome at the Cross Section of  $-90^\circ$  (Fuel Side)

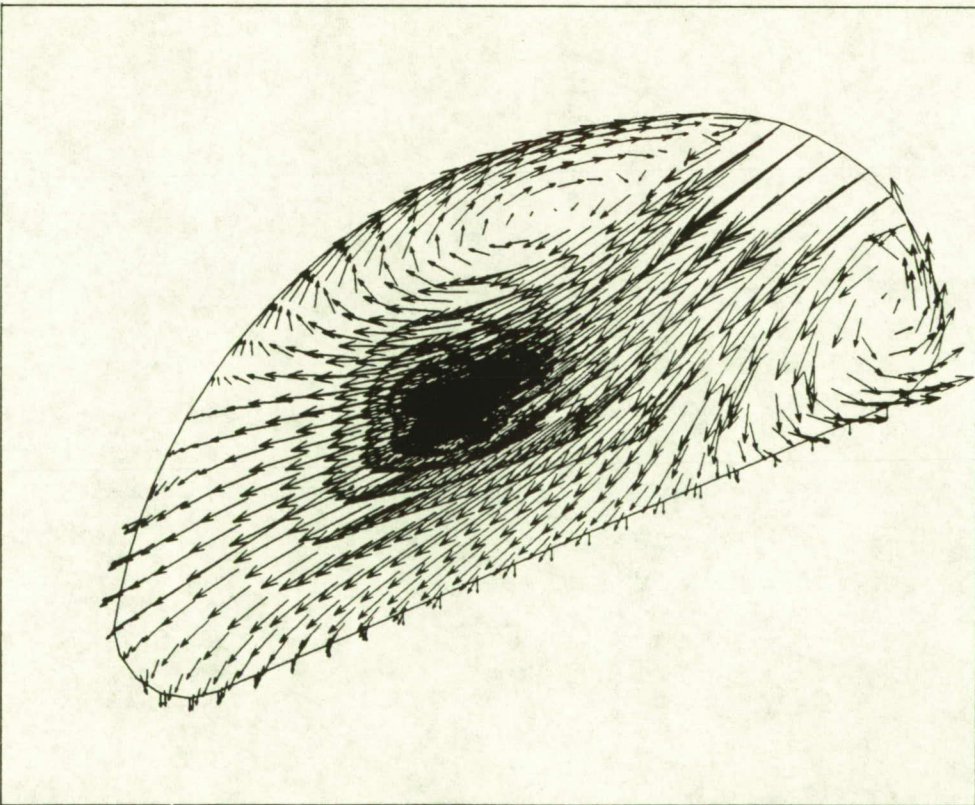


Figure 11b Velocity Vectors in the LOX Dome at the Cross Section of  $-2^\circ$



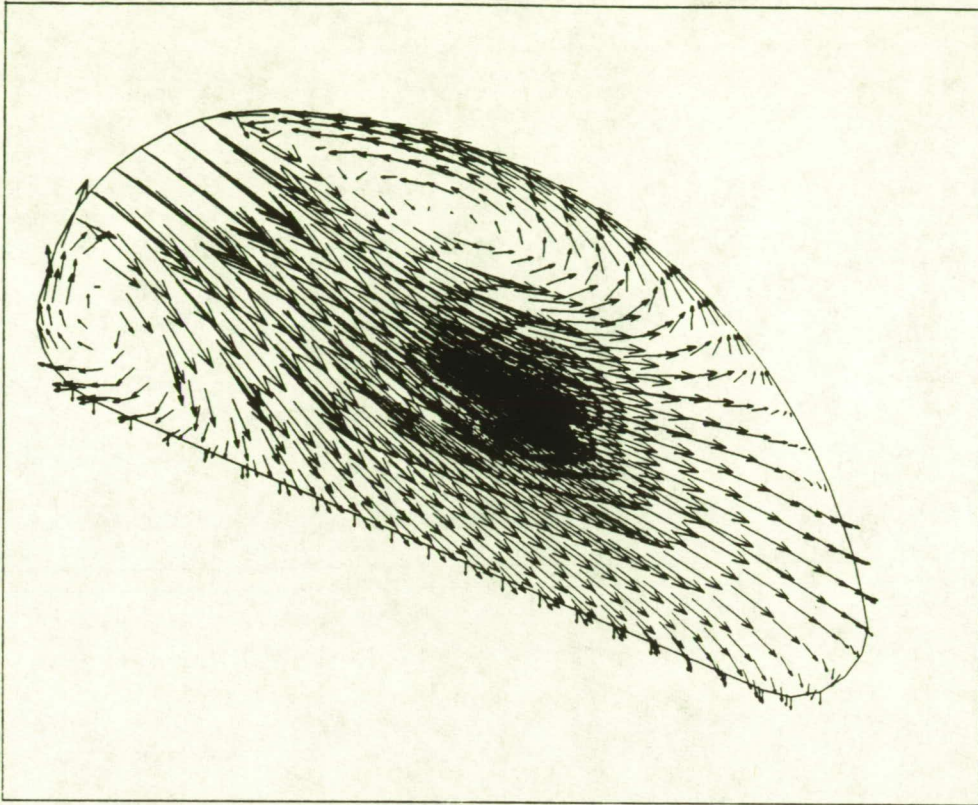


Figure 11c Velocity Vectors in the LOX Dome at the Cross Section of  $90^\circ$  (Oxidizer Side)

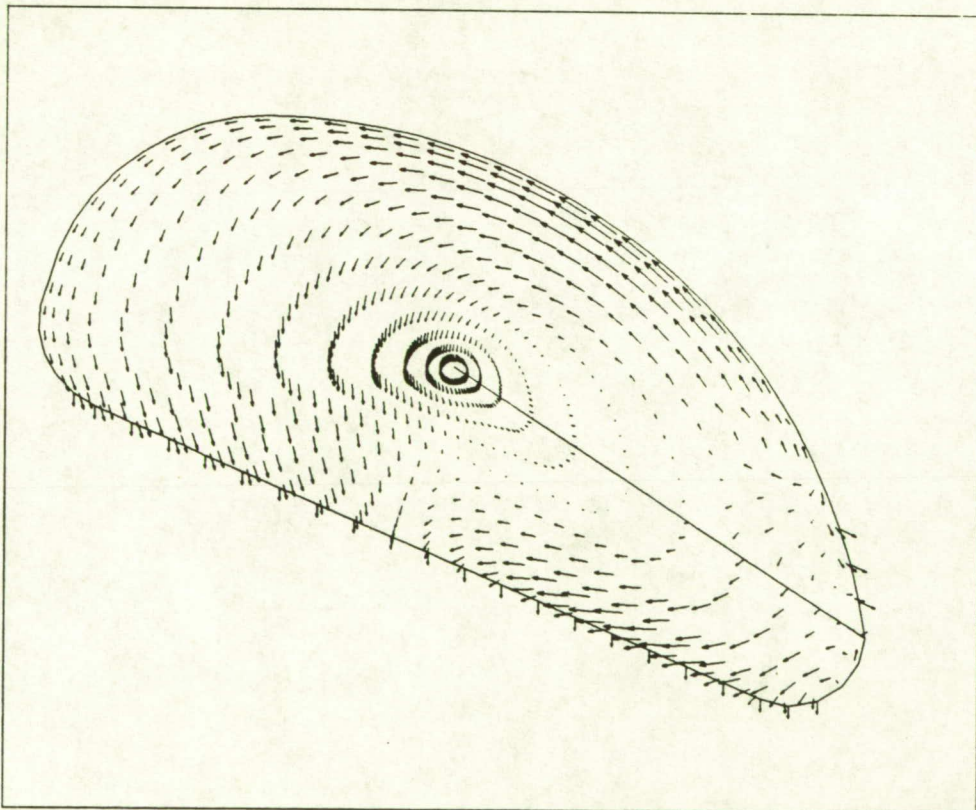


Figure 11d Velocity Vectors in the LOX Dome at the Cross Section of  $178^\circ$



in the plane without inlet flow. It can be seen that the exit flow velocities are fairly uniform in each cross section. The static pressure contours at the LOX dome exit plane are drawn in Figure 12. Although it seems higher pressure around the planes with inlet flow, the overall pressure difference is very small, which indicates a fairly uniform exit pressure. The contours of the exit velocity from the LOX dome to the injector face are plotted as shown in Figure 13, which demonstrate the same characteristics as that of the exit pressure.

## **4.2 HOT GAS INJECTOR ASSEMBLY**

The computational domain for the hot gas injector assembly consists of three zones: 1) LOX post assembly torus, 2) fuel transfer duct, and 3) oxidizer transfer duct. A  $37 \times 91 \times 25$  mesh system was employed for the LOX post assembly torus, and a  $10 \times 21 \times 17$  mesh system was used for the fuel transfer duct, while the oxidizer transfer duct was described by a  $10 \times 15 \times 15$  grid system. The geometry and the grid system of the hot gas injector assembly is plotted as shown in Figure 14. The inlet flow conditions to both transfer ducts are tabulated in Table 4. The inlet velocity and pressure profiles of the hot gas flow to the fuel transfer duct were interpolated based on the numerical results by Yang, and his coworkers (Ref. 15), while the inlet profiles to the oxidizer transfer duct were interpolated based on the image of Yang's results. The secondary velocity vectors of the inlet flows to the fuel transfer duct and the oxidizer transfer duct are sketched as shown in Figures 15a & 15b.

The loss coefficient distribution used in the LOX post assembly was based on the air flow test data for various post elements. The value of the loss coefficients is listed in Table 5.

A	5.2749E+05
B	5.2799E+05
C	5.2849E+05
D	5.2899E+05
E	5.2949E+05
F	5.2999E+05
G	5.3049E+05
H	5.3099E+05
I	5.3149E+05
J	5.3199E+05
K	5.3249E+05
L	5.3299E+05
M	5.3349E+05
N	5.3399E+05
O	5.3449E+05
P	5.3499E+05
Q	5.3549E+05
R	5.3599E+05
S	5.3649E+05
T	5.3699E+05
U	5.3749E+05
V	5.3799E+05
W	5.3849E+05
X	5.3899E+05
Y	5.3949E+05

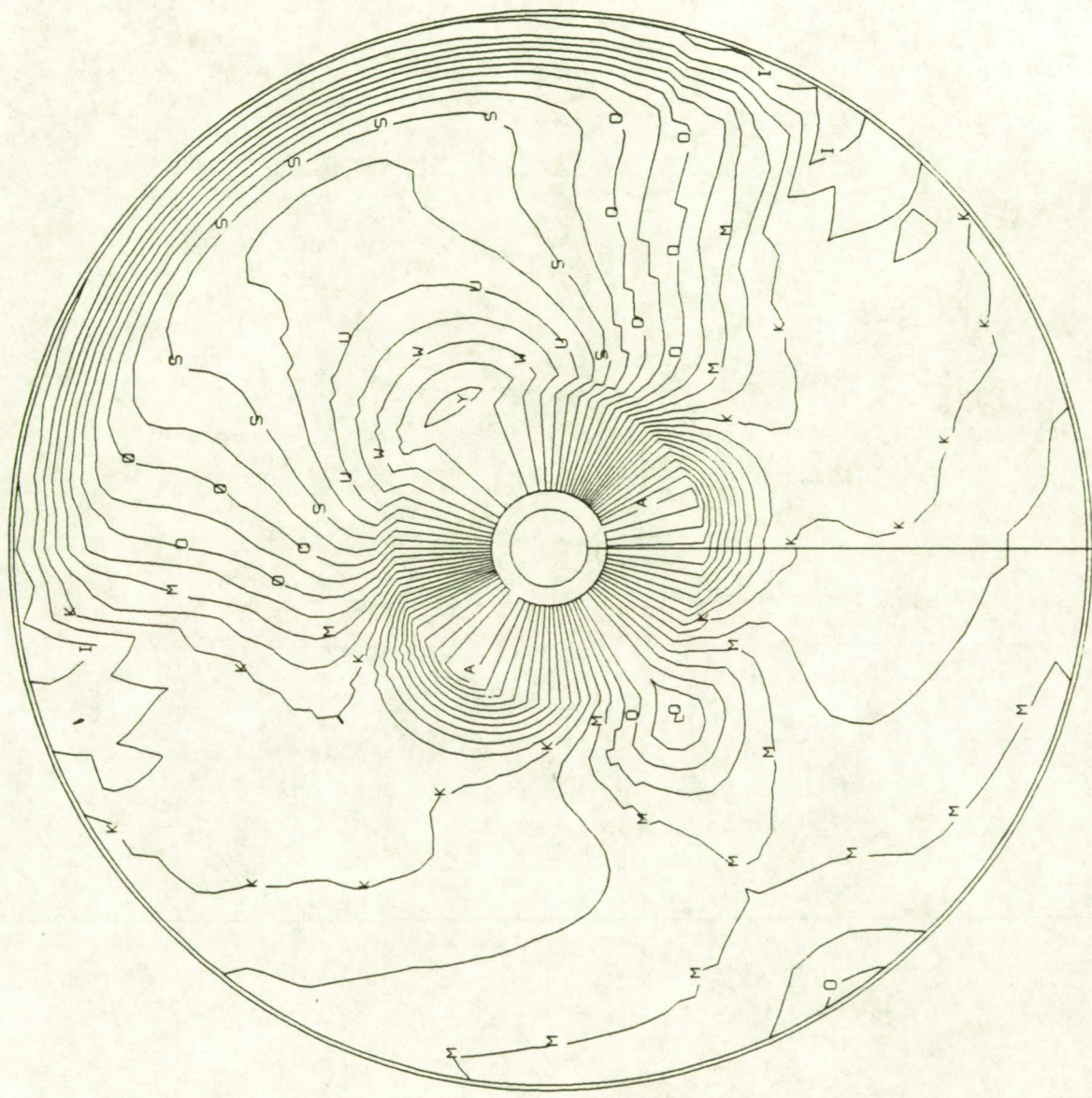


Figure 12 The Contours of Exit Pressure in the LOX Dome (psf)



A -7.5799E+00  
 B -7.5499E+00  
 C -7.5199E+00  
 D -7.4899E+00  
 E -7.4599E+00  
 F -7.4299E+00  
 G -7.3999E+00  
 H -7.3699E+00  
 I -7.3399E+00  
 J -7.3099E+00  
 K -7.2799E+00  
 L -7.2499E+00  
 M -7.2199E+00  
 N -7.1899E+00  
 O -7.1599E+00  
 P -7.1299E+00  
 Q -7.0999E+00  
 R -7.0699E+00  
 S -7.0399E+00  
 T -7.0099E+00  
 U -6.9799E+00

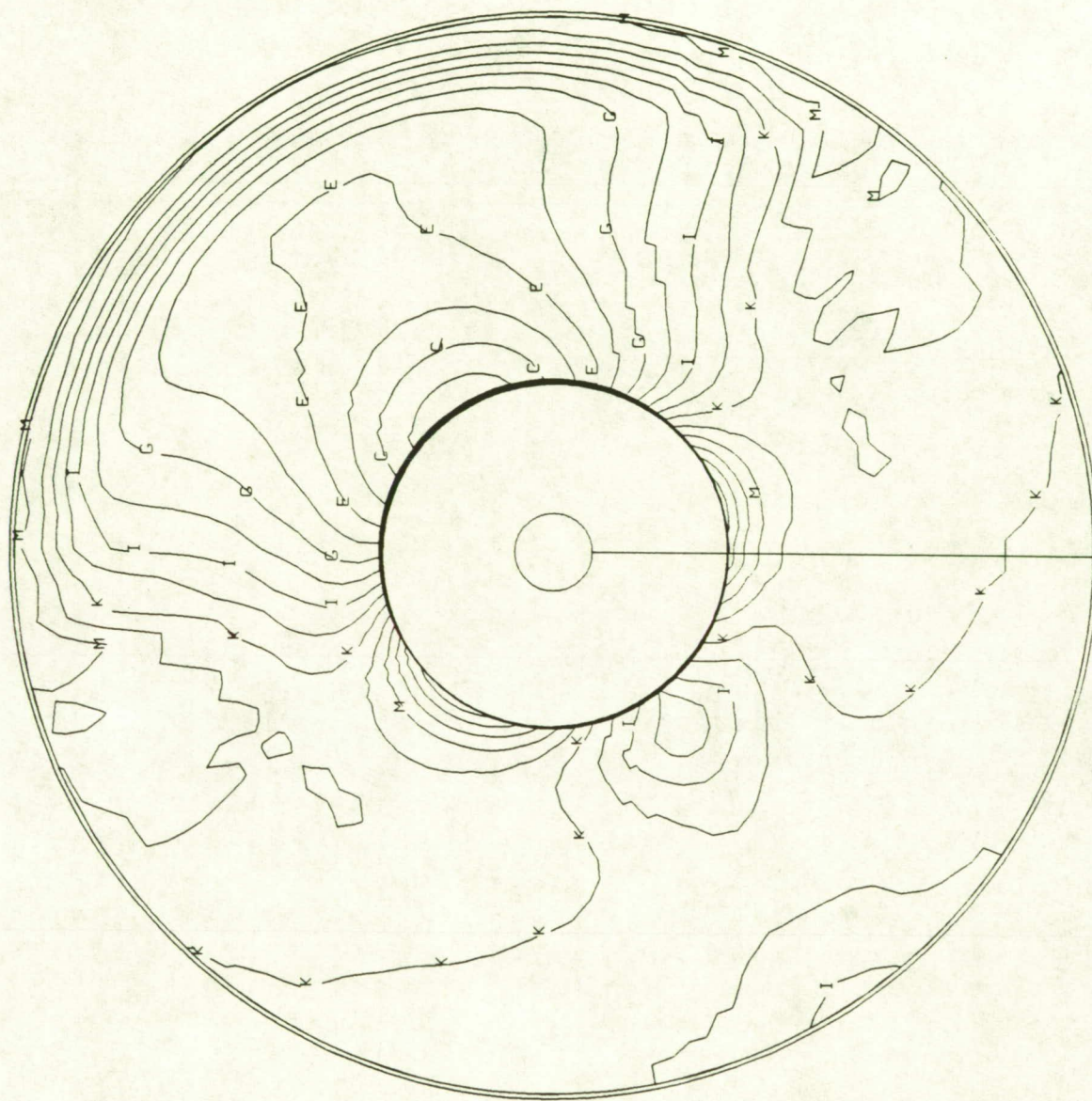


Figure 13 The Contours of Exit Velocity in the LOX Dome (ft/sec)

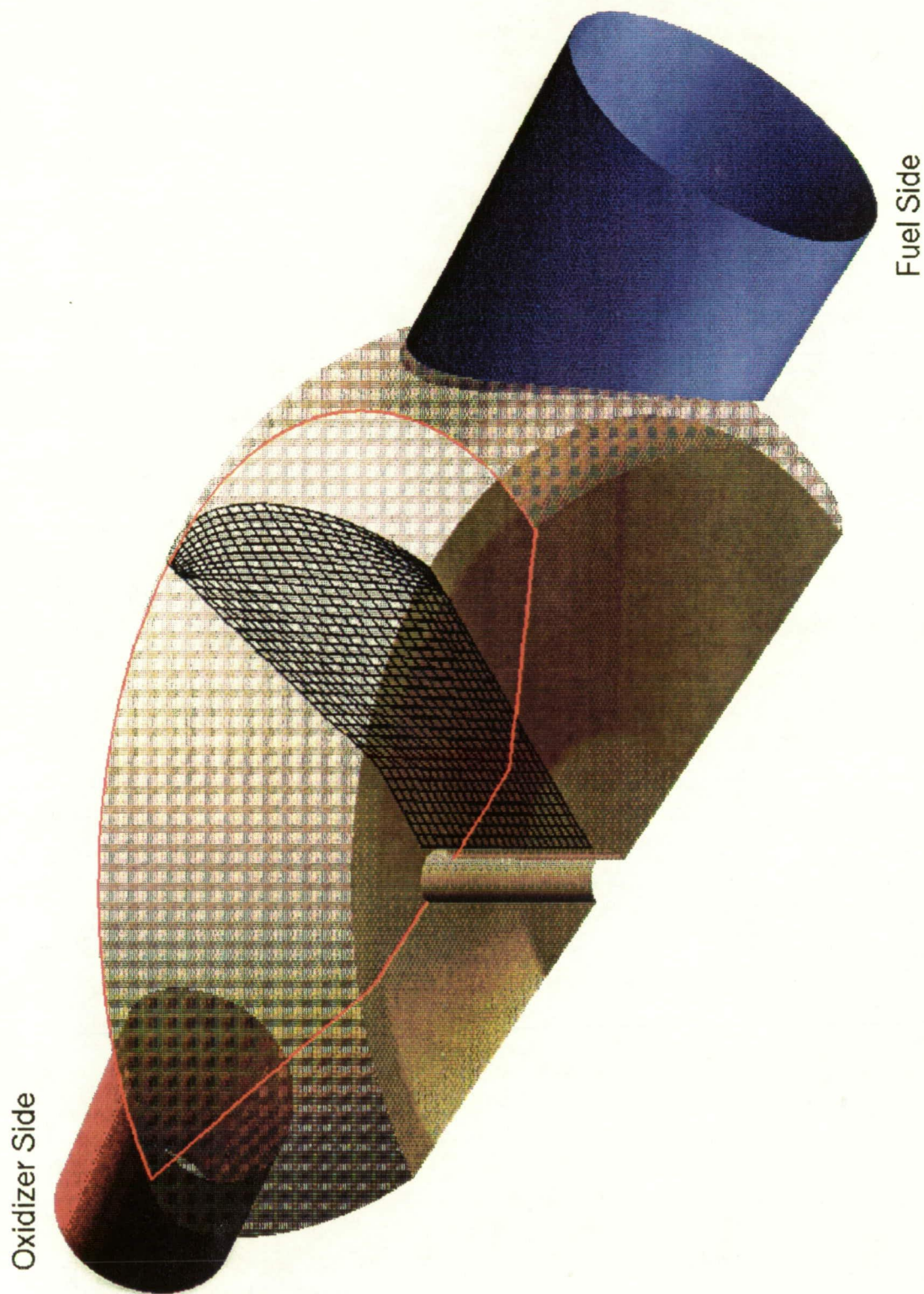


Figure 14 The Geometry and Grid System of the Hot Gas Injector Assembly



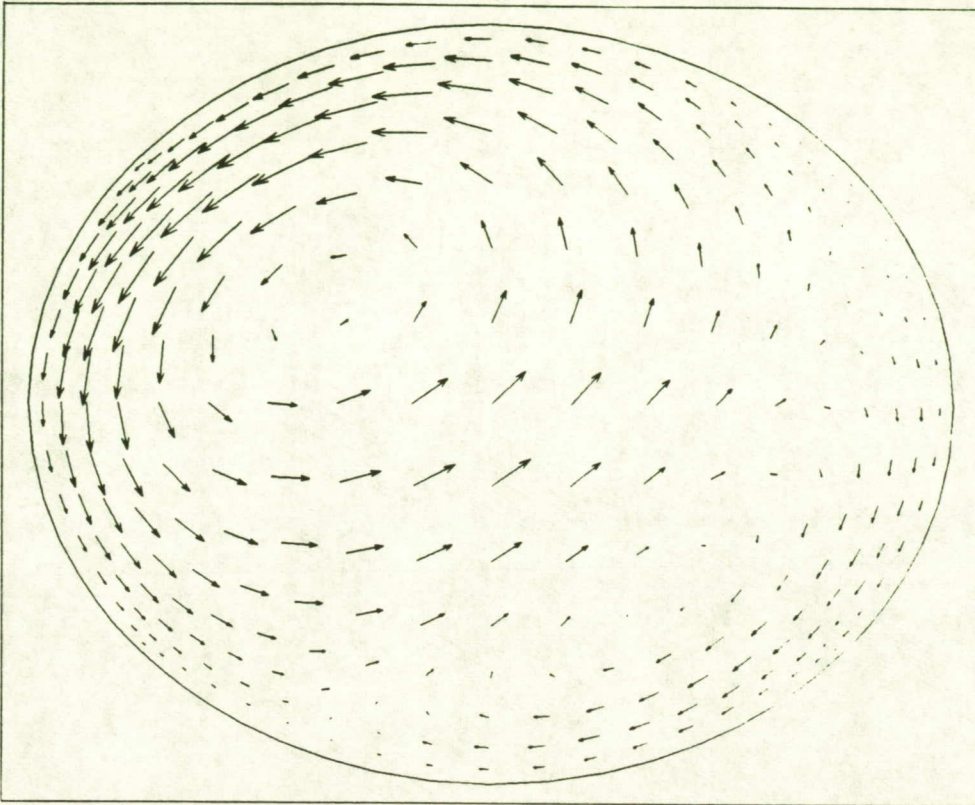


Figure 15a The Secondary Velocity Vectors of the Inlet Flow to the Fuel Transfer Duct

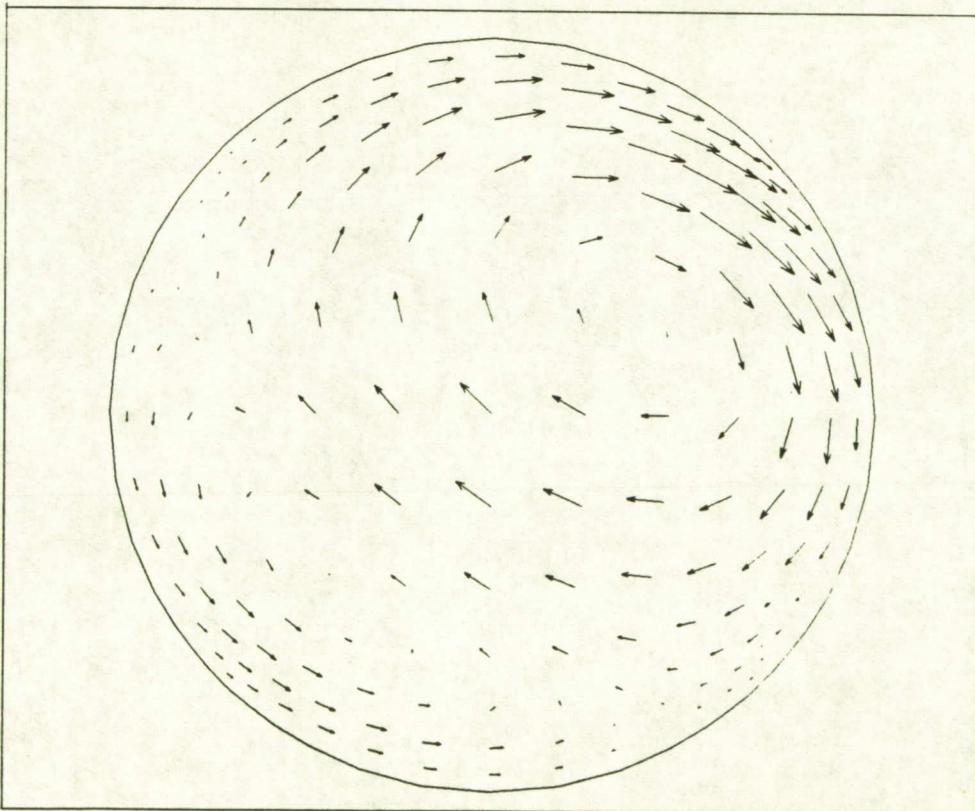


Figure 15b The Secondary Velocity Vectors of the Inlet Flow to the Oxidizer Transfer Duct



$K$  is the measured loss coefficient for each single post, while  $K'$  is the loss coefficient for each type of the posts in the computational domain. According to Equations (15-16), the relation between  $K$  and  $K'$  is

$$K' = \frac{\rho \Delta p}{\dot{M}^2} = \frac{\rho \Delta p}{(N \dot{m})^2} = \frac{K}{N^2} \quad (18)$$

where  $N$  is the number of each type of post elements.

Table 4 The Inlet Flow Conditions to the hot gas injector Assembly (104% RPL)

	Pressure (psi)	Temperature (°R)	Reynolds no. (ft <sup>-1</sup> )	Mass Flow Rate (lb/sec)	O/F Ratio
Fuel Side	3351	1666	$3.17 \times 10^7$	77.55 (in half)	0.8685
LOX Side	3353	1254	$7.88 \times 10^7$	33.38 (in half)	0.599

Table 5 The Loss Coefficients for the Hot Gas Flow Through the LOX Post

	Non-Baffle Elements			Baffle- Elements
	Row #13	Row #12	Row #1 - #11	
$K$ (in <sup>-4</sup> )	135	156	152	$\infty$
$K'$ (ft <sup>-4</sup> )	$4.374 \times 10^2$	$5.751 \times 10^2$	23	$\infty$

The numerical analysis for the hot gas injector assembly was conducted based on symmetrical, incompressible, isothermal, turbulent, no-reacting flow with two species (hydrogen and oxygen). Special attention was paid to the distribution of the porosity and of the drag coefficient on the 13th-row elements to identify the presence of holes on the shield. The predicted velocity vectors at the symmetrical plane are drawn as shown in Figure 16. It appears that the hot gas is deflected by the shielded elements (the outermost row), and passes through the non-shielded area of the posts. In addition, the exit velocity of the hot gas seems to be very uniform, except at the baffle elements through which there is no hot gas exit to the injector face. The deflected hot gas not only passes through the non-shielded area of the posts, but also sweeps around the torus, which can be seen from the velocity vector plots as shown in Figures 17-18. The hot gases from the fuel and the oxidizer sides flow into the region between the LOX posts and out into the main combustion chamber. The fuel side gases penetrate much further into a horizontal plane through the LOX-post region. Significant mixing occurs where the hot gases from the two sides of the engine meet. The exit velocity contours of the hot gas through the injector face are plotted in Figure 19. This figure shows that the exit velocity of the hot gas is somewhat larger near the fuel side than near the oxidizer side; however, the difference is very small which indicates that the flow is nearly uniform except at the baffle elements. The hot gas exit pressure contours on the bottom surface of hot gas injector assembly are plotted as shown in Figure 20, which exhibit the same characteristics as that of the exit velocity. The mixture ratio of the hot gas exit to the injector face is uniformly increased from the fuel side towards the oxidizer side as indicated in Figure 21, where the discontinuity at the symmetry plane is due to the linear extrapolation from interior points.

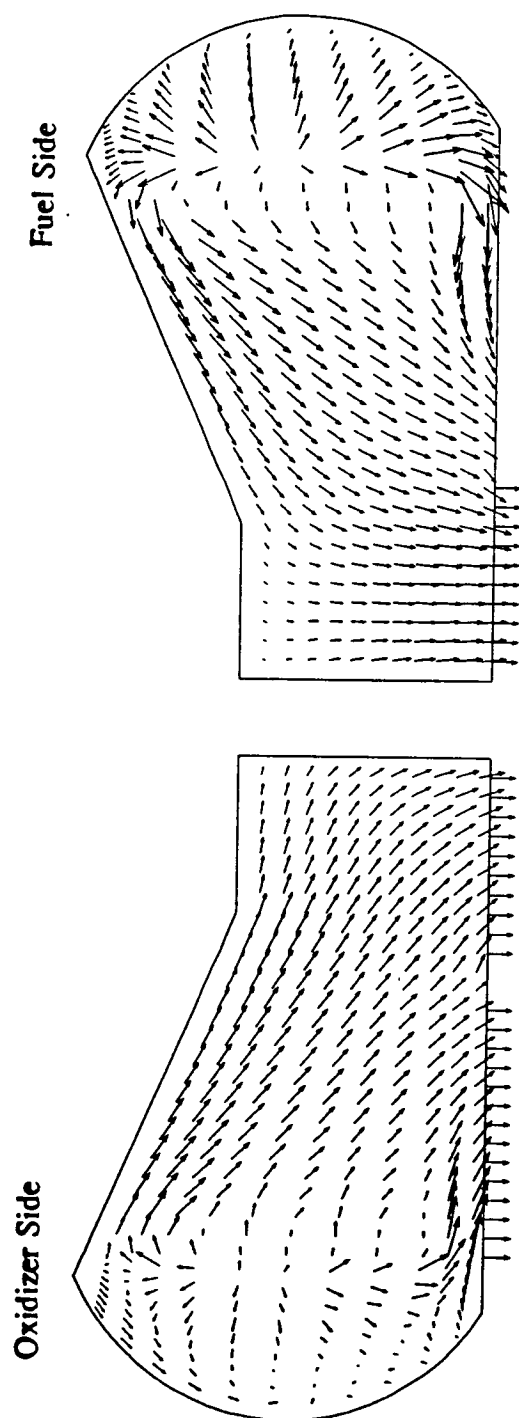


Figure 16 The Hot Gas Flow Velocity Vectors at the Symmetry Plane of LOX Post Assembly



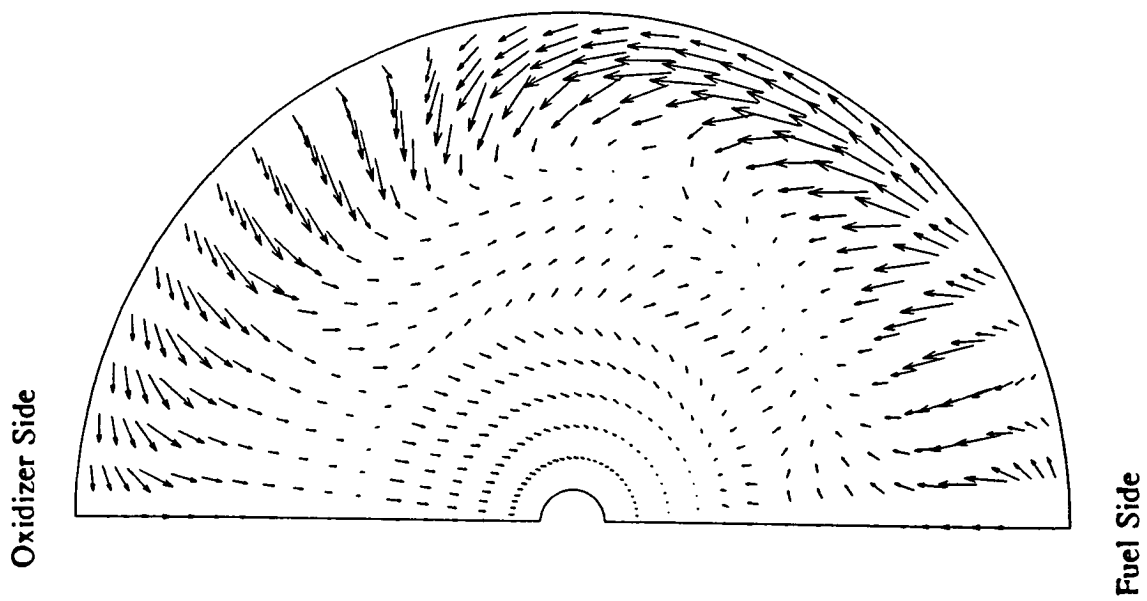


Figure 17 The Hot Gas Flow Velocity Vectors Near the Bottom Surface of LOX Post Assembly

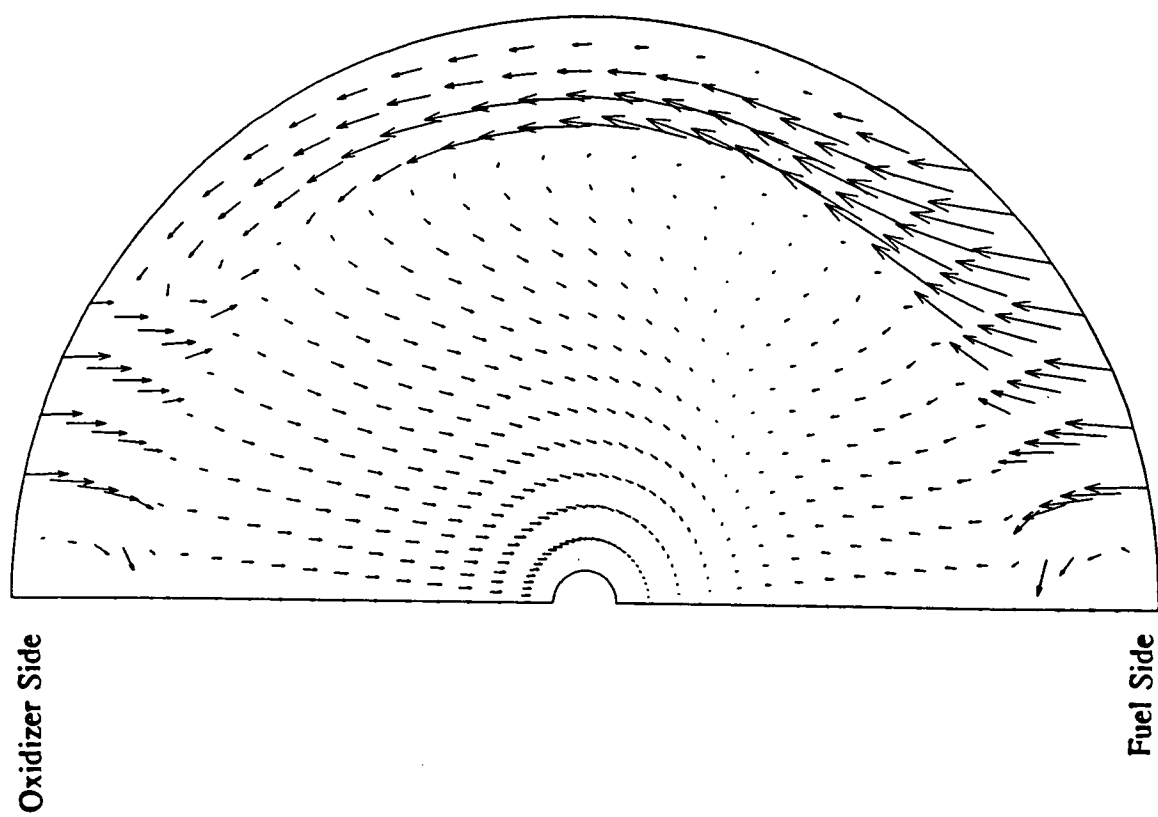


Figure 18 The Hot Gas Flow Velocity Vectors Near the Mid Plane of LOX Post Assembly

A -6.3999E+01  
 B -6.2999E+01  
 C -6.1999E+01  
 D -6.0999E+01  
 E -5.9999E+01  
 F -5.8999E+01  
 G -5.7999E+01  
 H -5.6999E+01  
 I -5.5999E+01  
 J -5.4999E+01  
 K -5.3999E+01  
 L -5.2999E+01  
 M -5.1999E+01  
 N -5.0999E+01  
 O -4.9999E+01  
 P -4.8999E+01

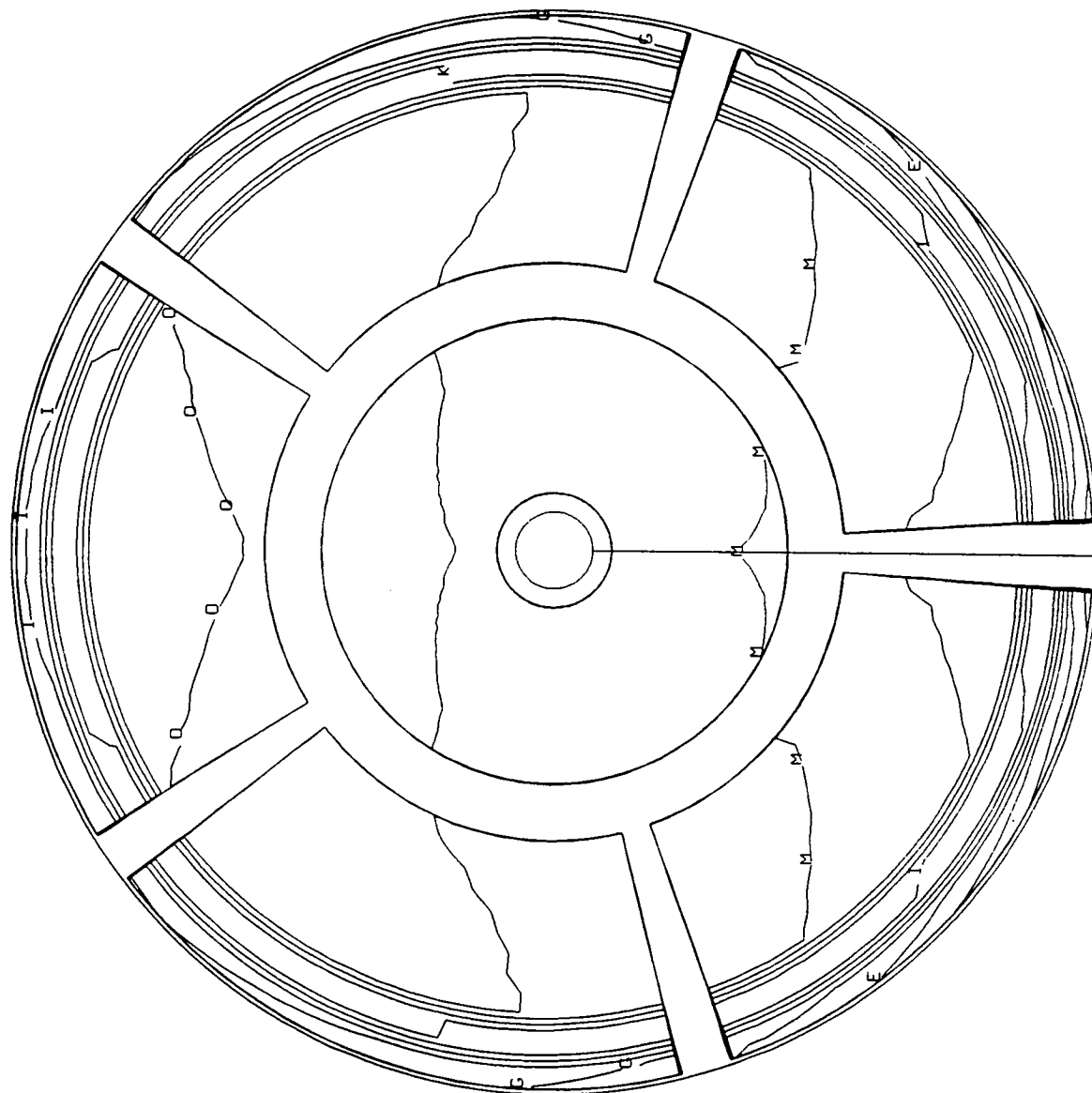


Figure 19 Hot Gas Exit Velocity Contours of the LOX Post Assembly (ft/sec)

CONTOUR LEVELS  
 472700.0  
 472800.0  
 472900.0  
 473000.0  
 473100.0  
 473200.0  
 473300.0  
 473400.0  
 473500.0  
 473600.0  
 473700.0  
 473800.0  
 473900.0  
 474000.0  
 474100.0  
 474200.0  
 474300.0  
 474400.0  
 474500.0  
 474600.0  
 474700.0  
 474800.0  
 474900.0  
 475000.0  
 475100.0  
 475200.0  
 475300.0  
 475400.0  
 475500.0

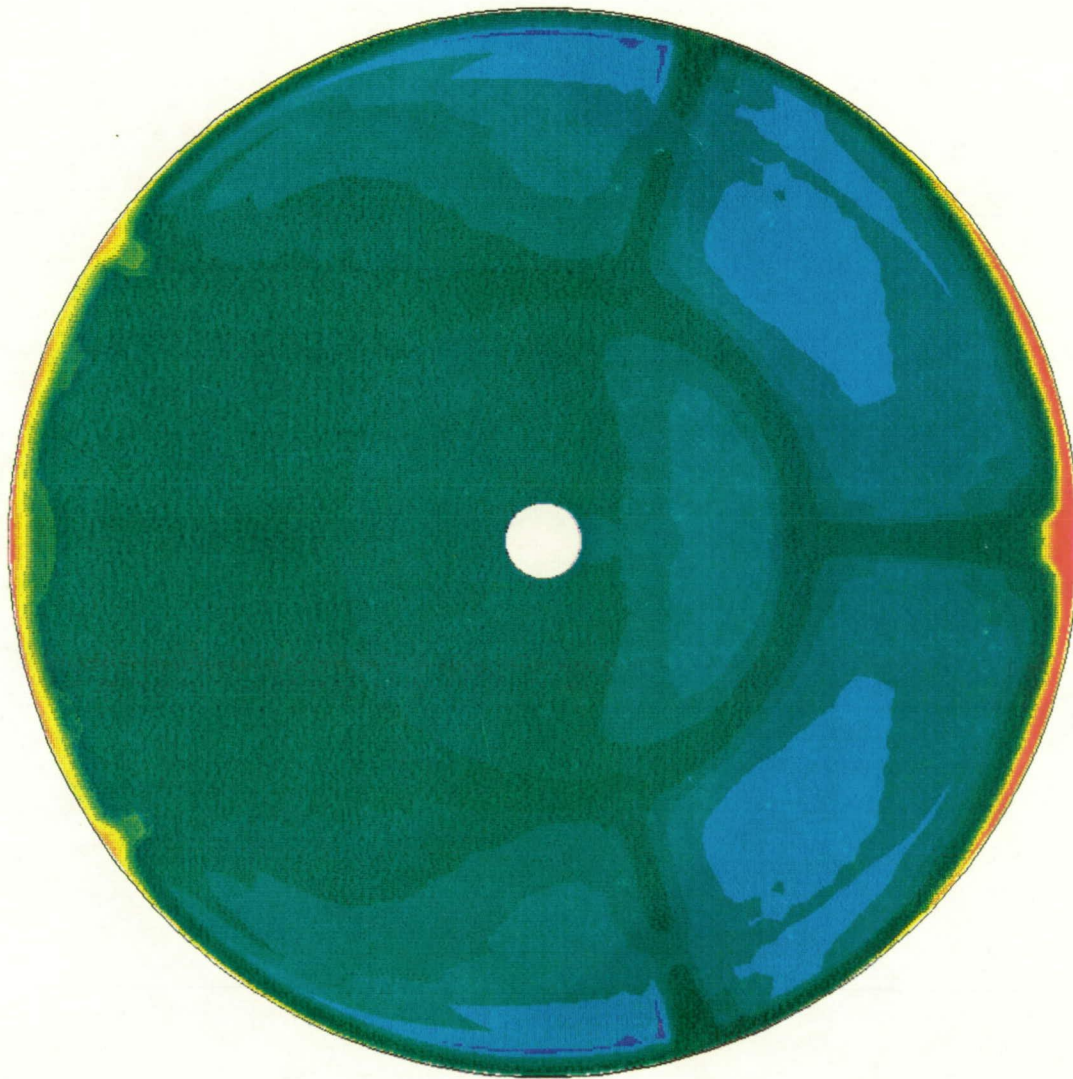


Figure 20 Hot Gas Exit Pressure Contours of the LOX Post Assembly (psf)



A	5.499E-01
B	5.649E-01
C	5.799E-01
D	5.949E-01
E	6.099E-01
F	6.249E-01
G	6.399E-01
H	6.549E-01
I	6.699E-01
J	6.849E-01
K	6.999E-01
L	7.149E-01
M	7.299E-01
N	7.449E-01
O	7.599E-01
P	7.749E-01
Q	7.899E-01
R	8.049E-01
S	8.199E-01
T	8.349E-01
U	8.499E-01

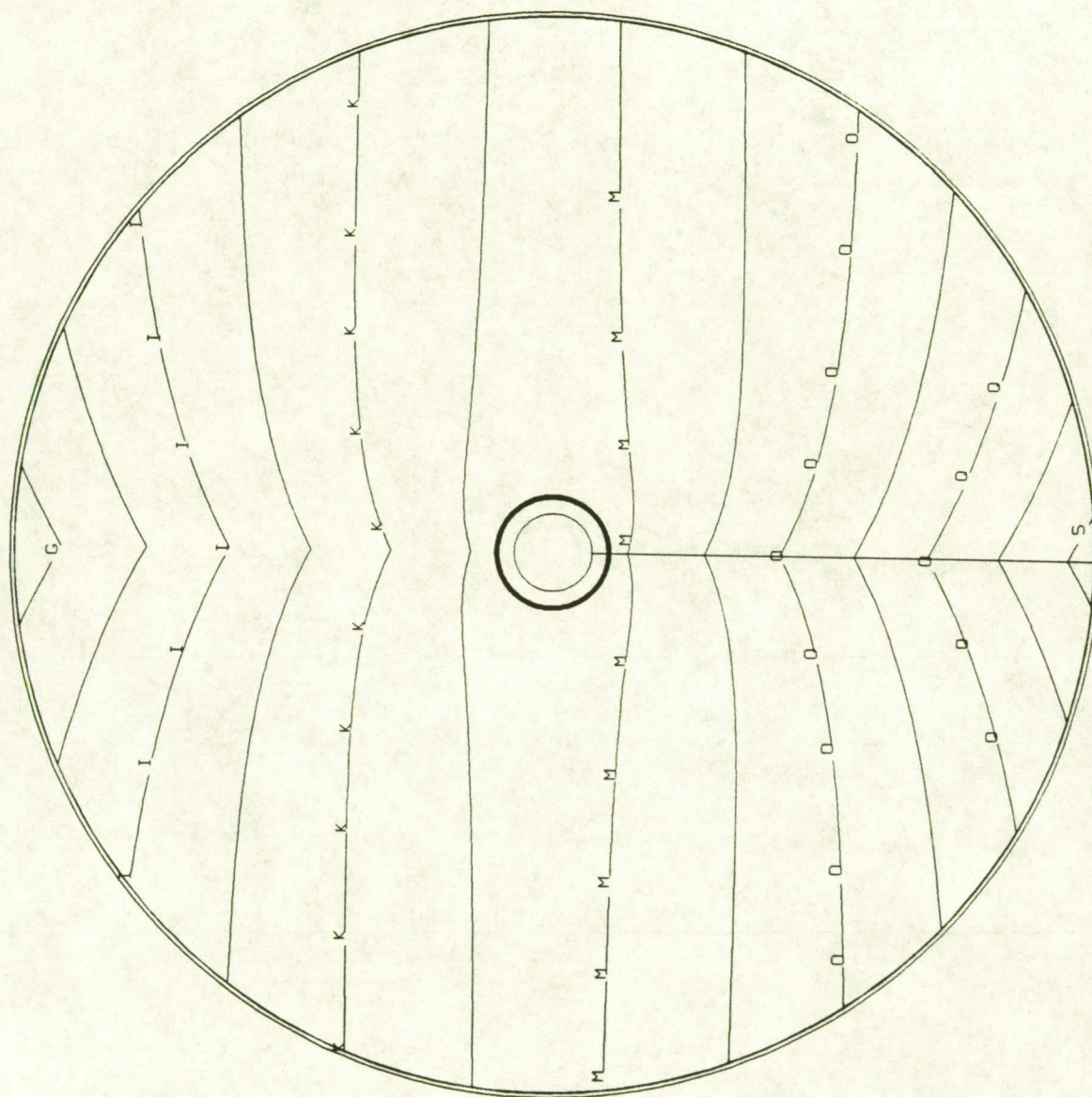


Figure 21 Hot Gas Exit O/F Ratio Contours of the LOX Post Assembly



### 4.3 HYDROGEN CAVITY

The hydrogen cavity region was discretized into a 29 x 91 x 14 mesh system, and is sketched as shown in Figure 22. The inlet flow conditions are listed in Table 6 based on 104% power balance. The inlet velocity profile was assumed to be uniform everywhere, and all velocity vectors were directed towards the center of radius.

Table 6 Inlet Conditions of the Fuel into Hydrogen Cavity Region (104% RPL)

Pressure (psi)	Temperature (°R)	Reynolds no. (ft <sup>-1</sup> )	Mass Flow Rate (lb/sec)
3395	449	$2.52 \times 10^7$	14.55 (in half)

The loss coefficient model is listed in Table 7, where the mass flow rate through each porous medium was based on 1-D analytical results. The back pressure of the secondary face plate was set to be 3288 psi from the hot gas injector assembly numerical result. An assumption was made that all hydrogen flow exiting through the secondary face plate to the hot gas region passed through the non-baffle elements and exited at the injector face. Therefore, in the post processing, the mass flow rate through the secondary face plate was added to the mass flow rate through the primary face plate at the same grid location.

The 3-D numerical analysis for the hydrogen cavity region was performed based on symmetrical, incompressible, adiabatic, turbulent flow with single species (hydrogen). The



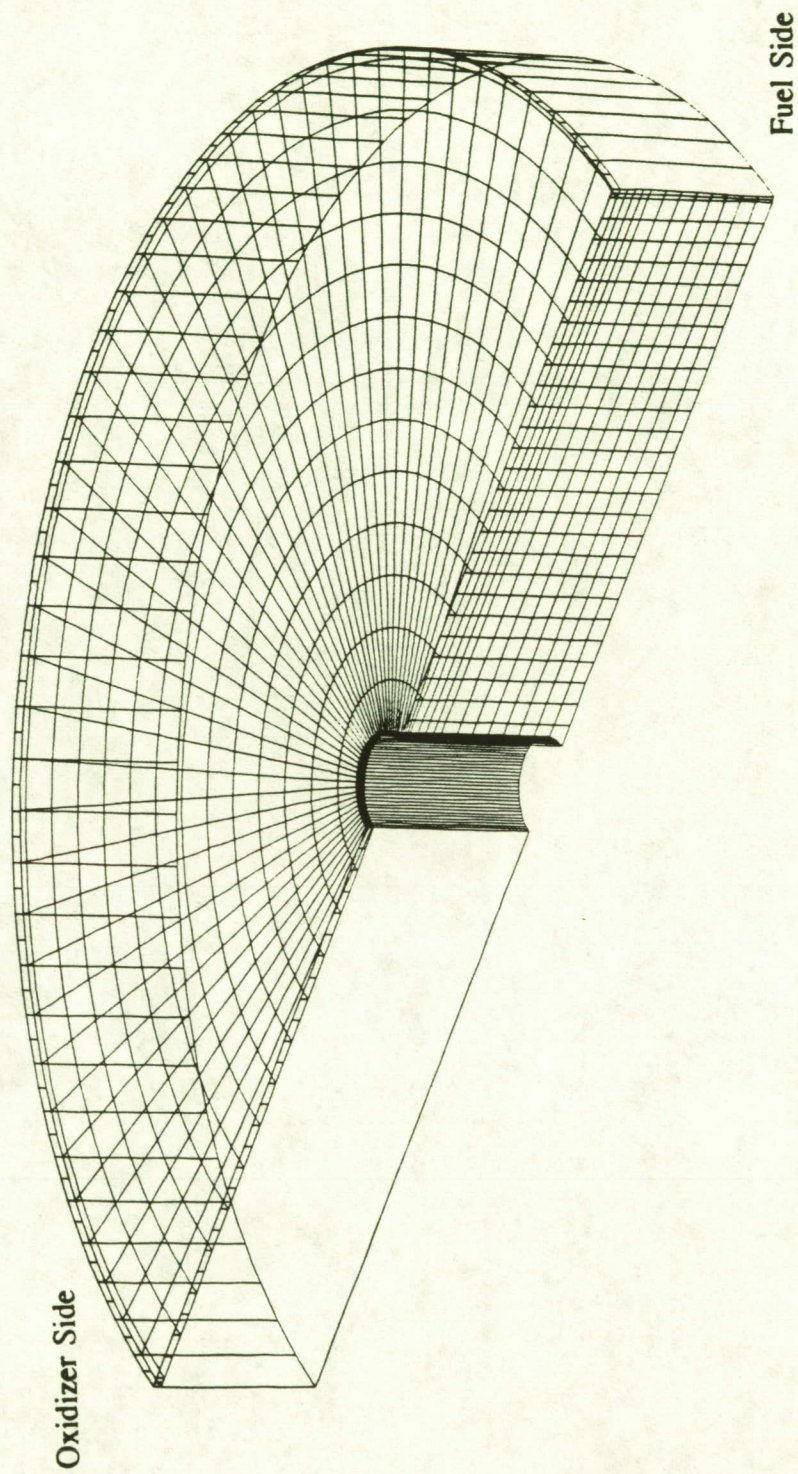


Figure 22 The Mesh System for the Hydrogen Cavity (29 x 91 x 14)



numerical result, as shown in Figure 23, indicates that a recirculation zone occurs as the fuel flow enters the hydrogen cavity through a narrow gap. It also reveals that the velocity of the flow exit through the baffle elements is quite uniform, and is much larger than that exit through porous plates. The flow exit through BLC holes has the largest velocity, but the exit mass flow rate is relatively small due to small exit area. The uniformity of the exit fuel flow can also be seen from the contours of the exit flow velocity and of the exit pressure in Figures 24 & 25, respectively.

Table 7 The Loss Coefficient Model Used in the Hydrogen Cavity Region (104% RPL)

	$\dot{m}$ (lb/sec)	$\Delta p$ (psi)	$K'$ (ft <sup>4</sup> )
Primary Face Plate	6.77	251	$3.578 \times 10^4$
Secondary Face Plate	3.41	98	$5.506 \times 10^4$
Baffle Elements	15.25	301	$8.467 \times 10^3$
Non-Baffle Elements	0	251	$\infty$
BLC Holes	3.67	251	$1.16 \times 10^5$



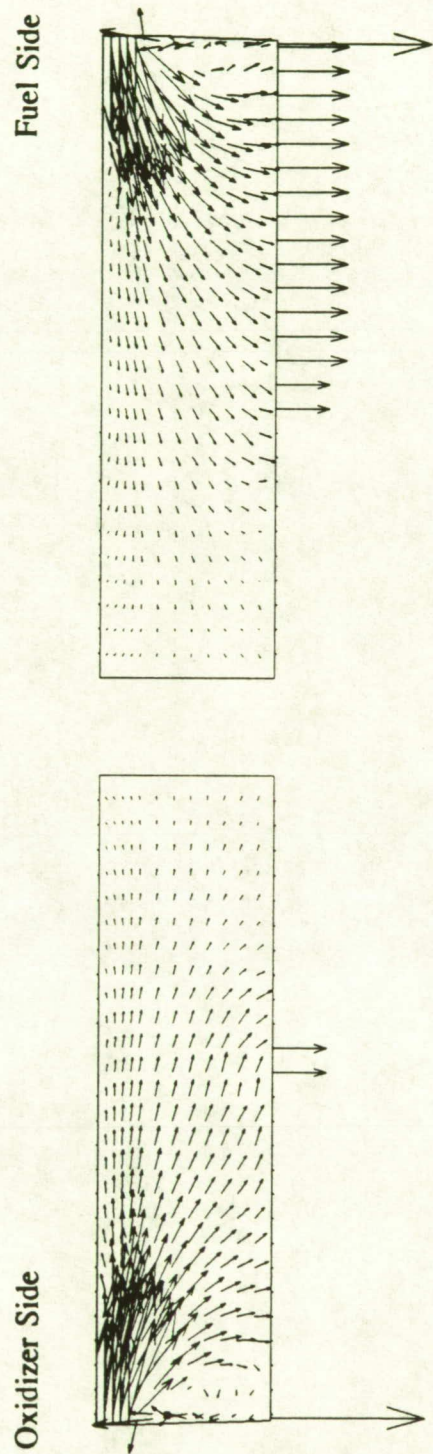
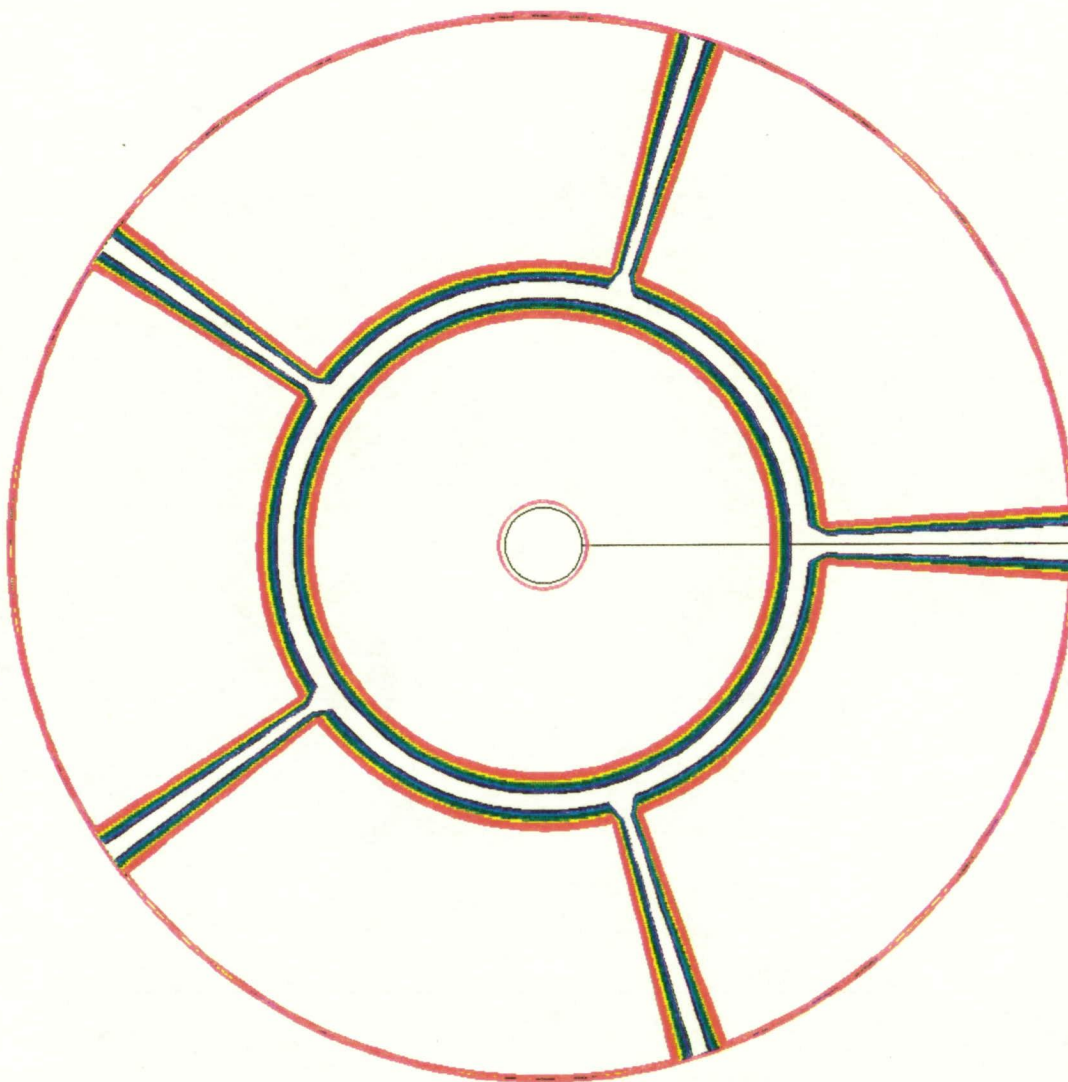


Figure 23 The Velocity Vectors of the Fuel Flow at the Symmetry Plane of the Hydrogen Cavity

Hydrogen Cavity, Exit Flow Velocity Contours (ft/sec)



CONTOUR LEVELS

-61.0  
-58.0  
-55.0  
-52.0  
-49.0  
-46.0  
-43.0  
-40.0  
-37.0  
-34.0  
-31.0  
-28.0  
-25.0  
-22.0  
-19.0  
-16.0  
-13.0  
-10.0  
-7.0  
-4.0  
-1.0

Figure 24 The Contours of the Exit Flow Velocity in the Hydrogen Cavity (ft/sec)



A 4.8798E+05  
 B 4.8800E+05  
 C 4.8802E+05  
 D 4.8804E+05  
 E 4.8806E+05  
 F 4.8808E+05

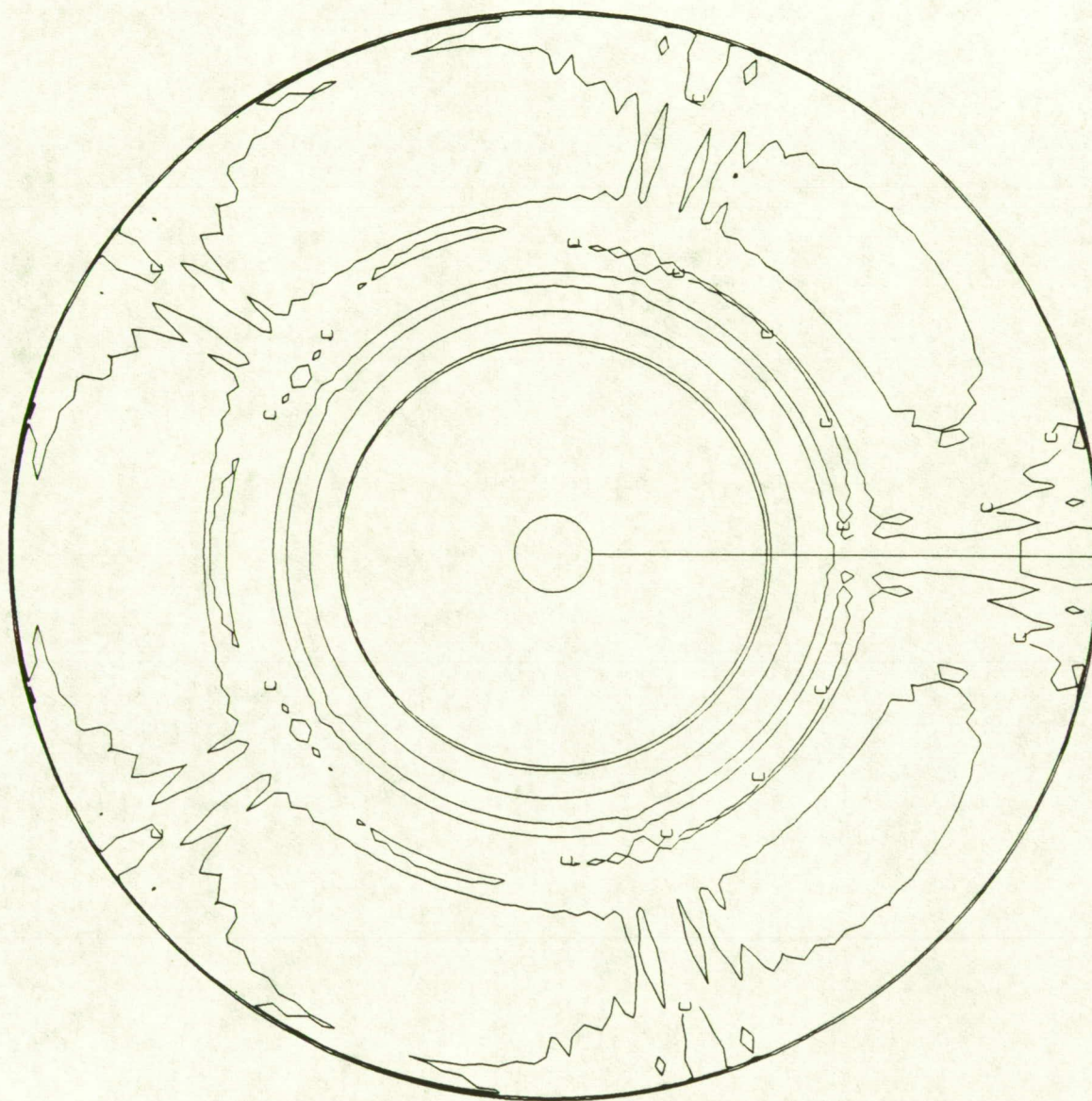
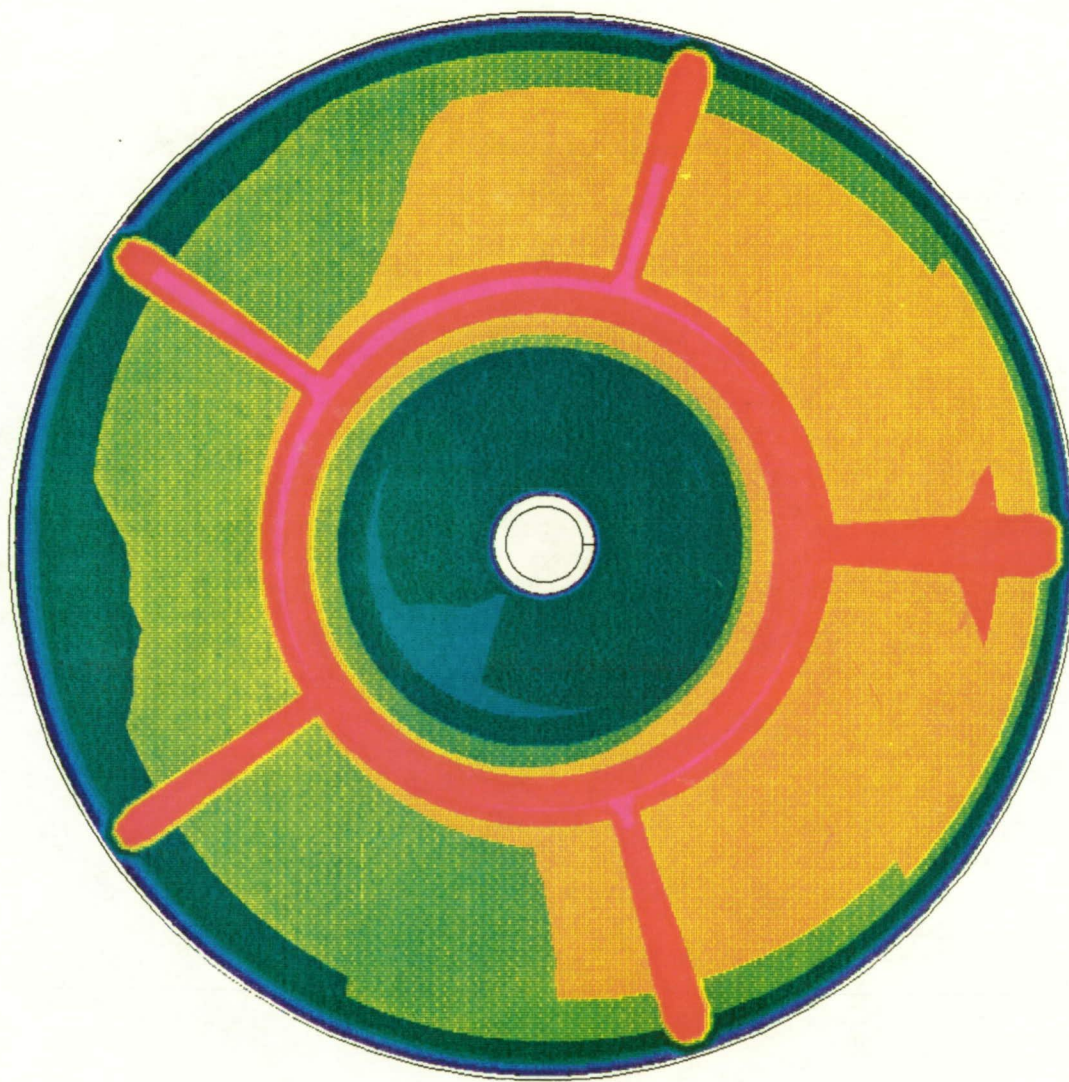


Figure 25 The Contours of the Exit Pressure in the Hydrogen Cavity (psf)

#### 4.4 MAIN INJECTOR ASSEMBLY

After conducting the numerical computation for the three components of the main injector assembly, a post processing calculation was made in order to obtain the overall O/F ratio at the injector face. By superimposing the exit mass flow rates and the mass fractions of hydrogen and oxygen from the three components of the main injector assembly, the mixture ratio distribution at the injector face was obtained as shown in Figure 26. It appears that the highest O/F ratio occurs near the baffle elements. The O/F ratio distribution also exhibits higher mixture ratio near the fuel side than that near the oxidizer side. The O/F distribution in the circumferential direction is of great interest, especially near the outer edge of the injector face, and so it is plotted as shown in Figures 27 & 28, respectively. Figure 27 plots the value without adding BLC coolant flow in the O/F ratio calculation, while Figure 28 shows the O/F ratio with BLC coolant flow added. Each spike in the mixture ratio plots occurs at baffle elements. The O/F ratio distribution in the radial direction is displayed in Figures 29 & 30, which shows the mixture ratio at the plane of  $-90^\circ$  (on the fuel side) and  $90^\circ$  (on the oxidizer side), respectively. The plots reveal that the O/F ratio is close to stoichiometric around baffle elements.





CONTOUR LEVELS  
 3.0  
 3.5  
 4.0  
 4.5  
 5.0  
 5.5  
 6.0  
 6.5  
 7.0  
 7.5  
 8.0  
 8.5

Figure 26 The O/F Ratio Contours of the Main Injector Assembly at 104% Power Level

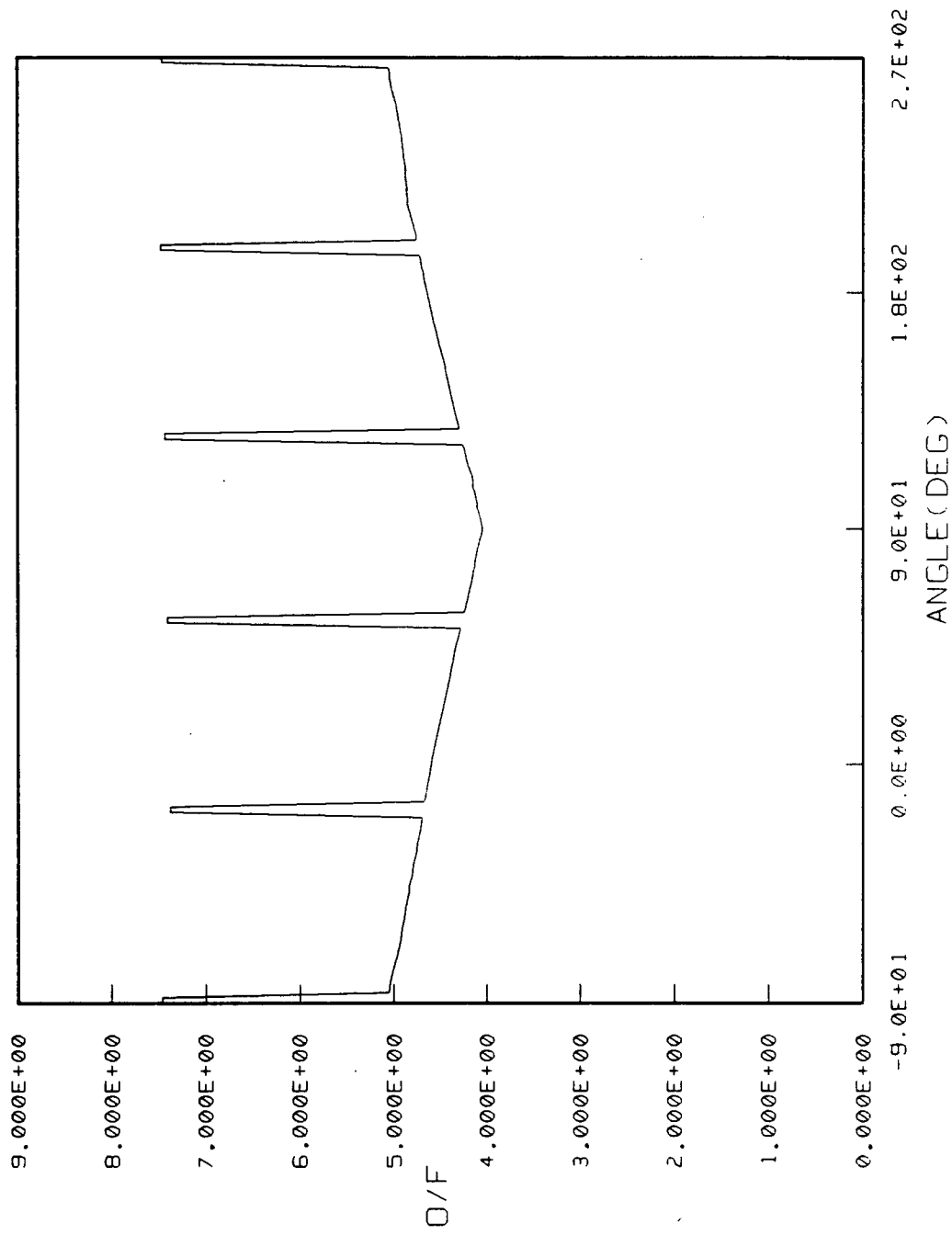


Figure 27 The O/F ratio Distribution Along the Outer Edge of the Injector Face (no BLC Coolant Added)

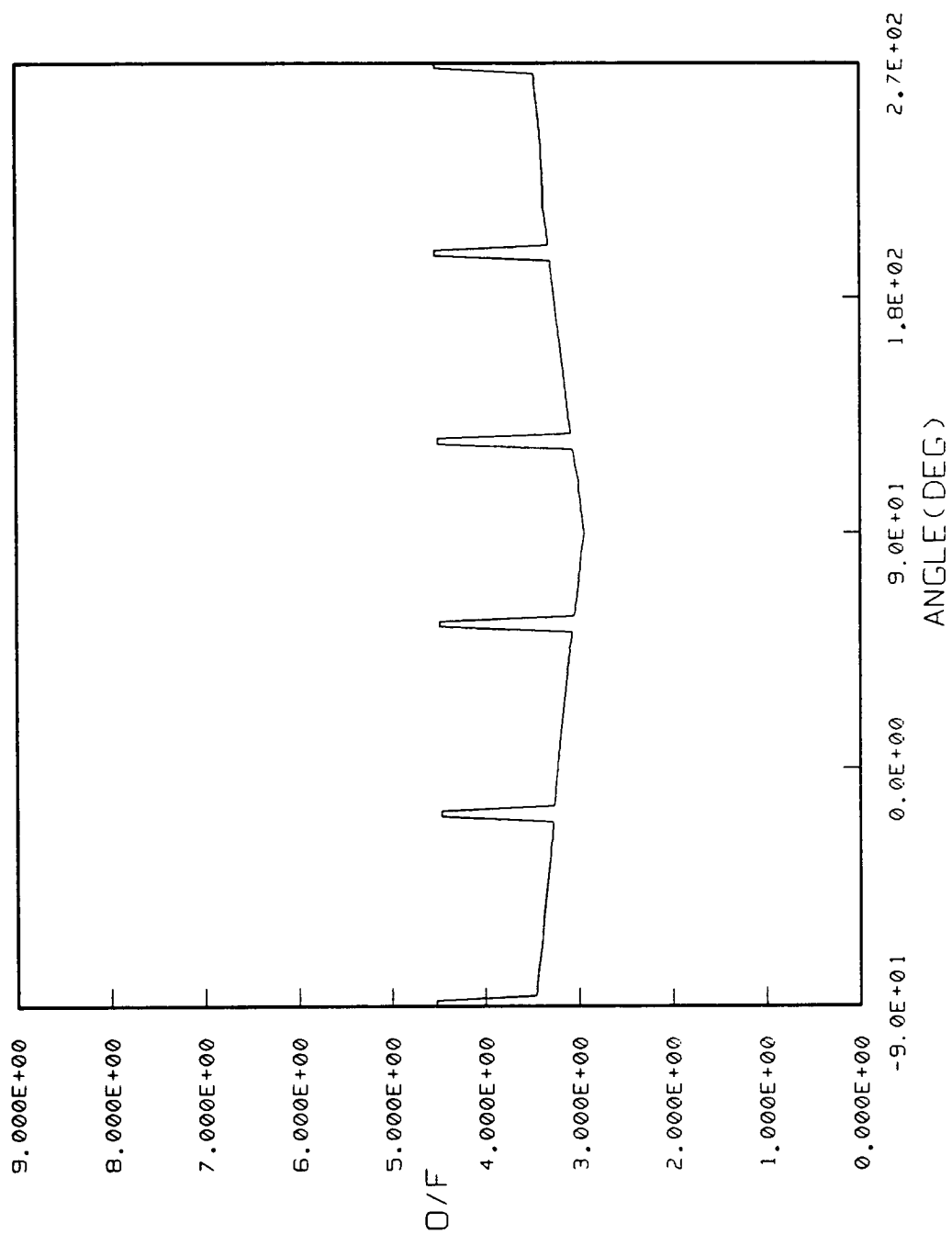


Figure 28 The O/F ratio Distribution Along the Outer Edge of the Injector Face (BLC Coolant Added)

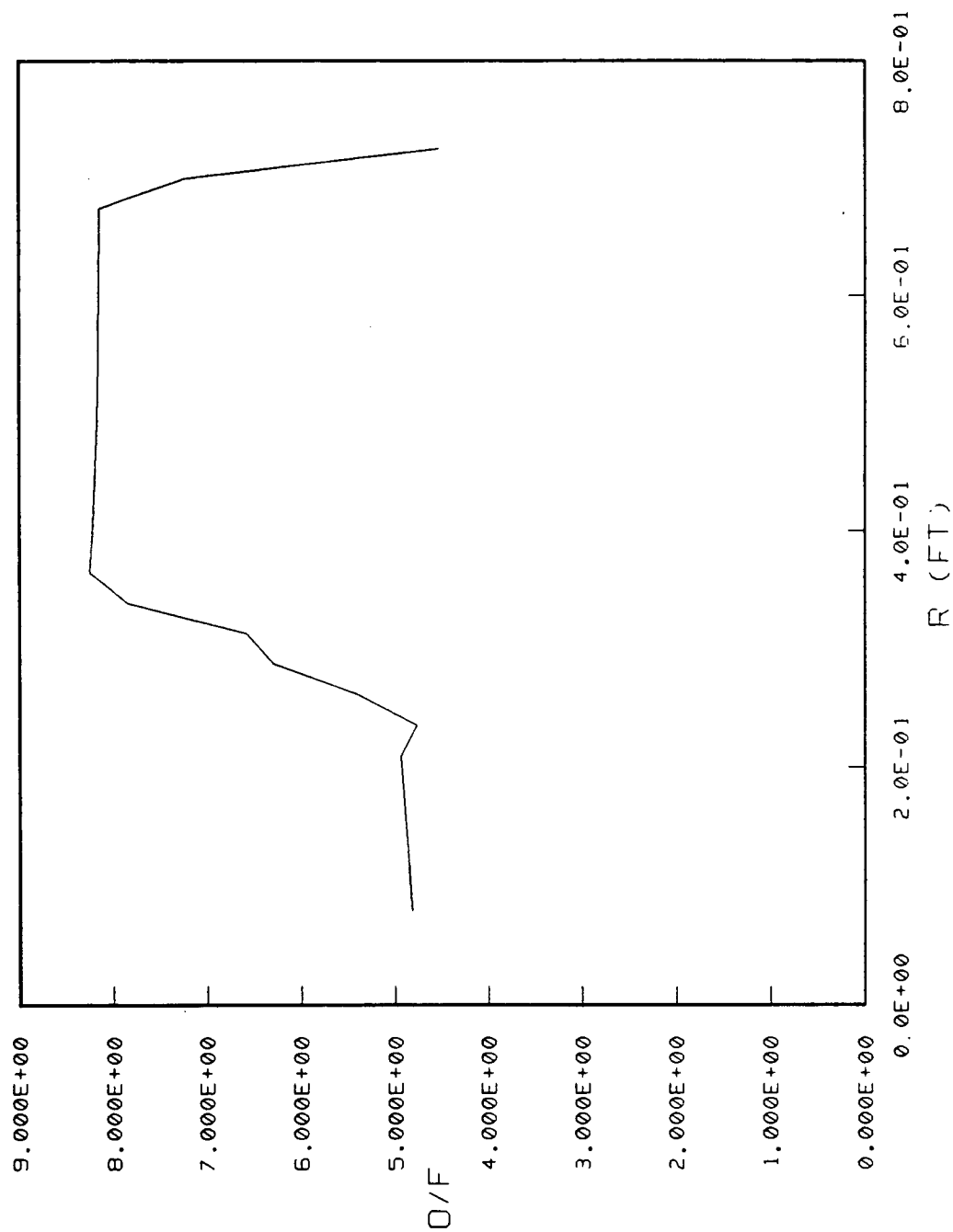


Figure 29 The O/F Ratio Distribution at -90° (Fuel Side) of the Injector Face (with BLC Coolant Added)



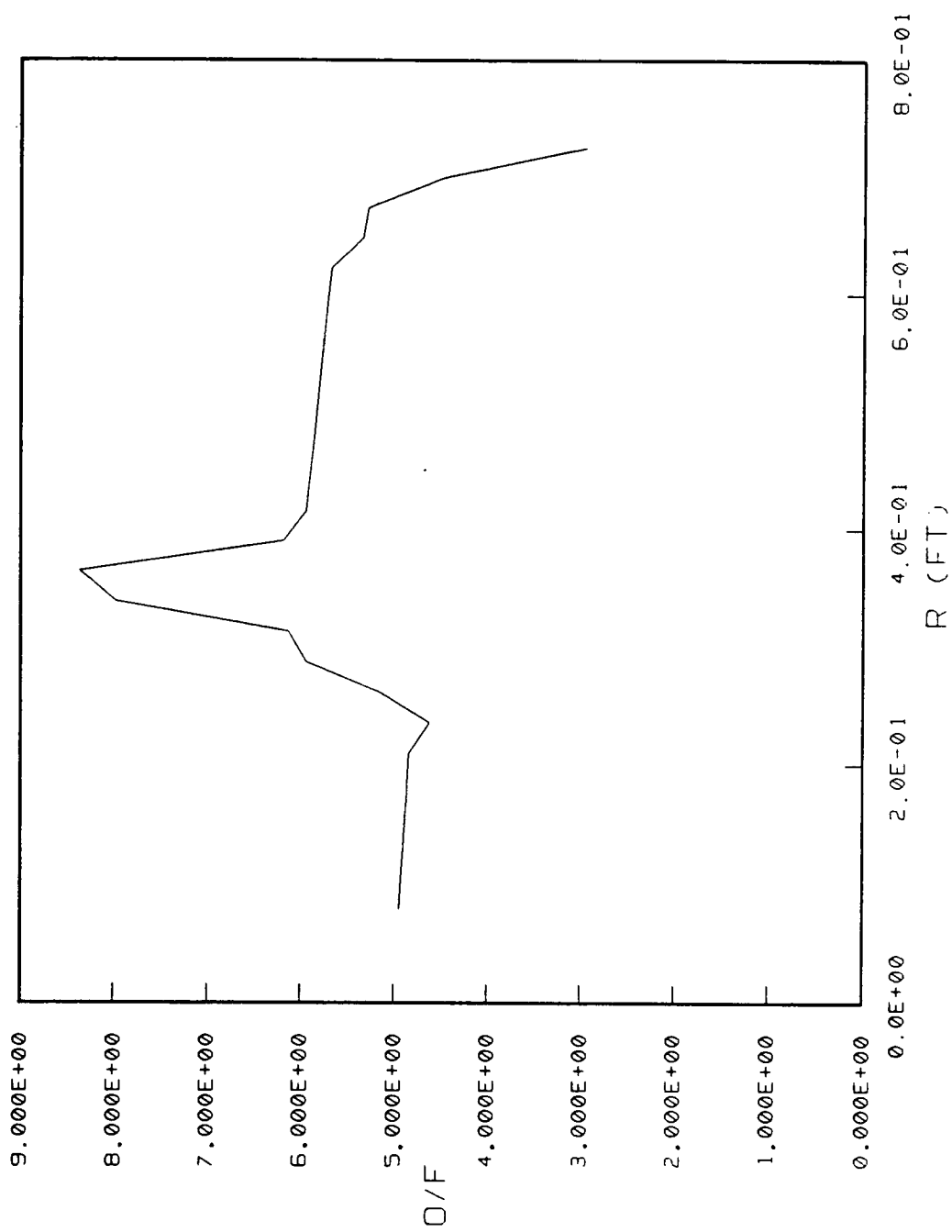


Figure 30 The O/F Ratio Distribution at 90° (Oxidizer Side) of the Injector Face (with BLC Coolant Added)

## 5.0 CONCLUSIONS AND RECOMMENDATIONS

The 3-D CFD/porosity analysis reveals that the mass flow rate at the injector face is relatively uniform. The predicted mixture ratio is close to stoichiometric ( $O/F = 8$ ) around baffle element at 104% power balance level, which might cause very hot spots around baffle elements. However, due to the many assumptions made in the porosity model and the use of a very coarse grid system, the numerical results can only provide a qualitative trend. As can be seen from the loss coefficient model, the local mass flow rate distribution is dependent on both the pressure drop and the loss coefficient distributions. Hence, the assembly of the loss coefficient model is critical to the numerical result, and the availability of the measured loss coefficients for each porous medium will greatly improve the CFD analysis. In addition, the distribution of chamber pressure and of baffle element discharge pressure was assumed to be uniform in this study; hence, the CFD/porosity model can be improved if the actual distribution of discharge pressure were known and specified in the calculation. Meanwhile, a proper inlet flow profile to the LOX dome and to the hydrogen cavity can help the developed model to predict the flow field more accurately. The developed CFD/porosity model should be further tested at different power balance levels. The numerical results of this study should be used as the inlet conditions to the combustion chamber in order to predict the engine performance and heat loads of the chamber.

## REFERENCES

1. **Sha, W.T.**, "Summary of Methods Used in Rod-Bundle Thermal-Hydraulic Analysis," in Turbulent Force Convection in Channels and Bundles, Vol. 1, Ed. S. Kakac and D.B. Spalding, McGraw-Hill International Book Company, pp. 279-299, 1979.
2. **Soo, S.L.**, and **Sa, W.T.**, "Porous Medium Formulation of Three-Dimensional Transient Flow Through Rod Bundles," in Turbulent Force Convection in Channels and Bundles, Vol. 1, Ed. S. Kakac and D.B. Spalding, McGraw-Hill International Book Company, pp. 301-323, 1979.
3. **Sha, W.T.**, and **Thompson, J.F.**, "Rod-Bundle Thermal Hydraulic Analysis Using Boundary Fitted Coordinate System," NUREG-CR-0001, ANL-78-1, Jan. 1978.
4. **Coucaud, O.**, **Morel, P.**, and **Caltagirone, J.P.**, "Numerical Modeling on Non-Linear Effects in Laminar Flow Through a Porous Medium," Journal of Fluid Mechanics, Vol. 190, 1988, pp. 393-407.
5. **Chen, Y.S.**, "Viscous Flow Computations Using a Second-Order Upwind Differencing Scheme," AIAA Paper 88-0417, AIAA 26th Aerospace Sciences Meeting, Reno, Nevada, Jan. 1988.
6. **Chen, Y.S.**, "Compressible and Incompressible Flow Computations with a Pressure Based Method," AIAA Paper 89-0286, AIAA 27th Aerospace Sciences Meeting, Reno, Nevada, Jan. 1989.
7. **Chen, Y.S.**, "3-D Stator-Rotor Interaction of the SSME," AIAA Paper 88-3095, AIAA/ASME/SAE/ASEE 24th Joint Propulsion Conference, Boston, MA, July 1988.
8. **Chen, Y.S.**, and **Kim, S.W.**, "Computation of Turbulent Flows Using an Extended k- $\epsilon$  Turbulence Model," NASA CR-179204, Oct. 1987.
9. **White, F.M.**, Heat and Mass Transfer, Addison-Wesley Publishing Co., Inc., 1988.
10. **Stasiulevičius, J.**, and **Skrinska, A.**, Heat Transfer of Finned Tube Bundles in Crossflow, Hemisphere Publishing Co., New York, 1988.
11. **Žukauskas, A.**, and **Ulinskas, R.**, Heat Transfer in Tube Banks in Crossflow, Hemisphere Publishing Co., New York, 1988.
12. **Žukauskas, A.A.**, and **Kalinlin, E.K.**, "Enhancement of Heat Transfer," in Heat Transfer Soviet Reviews, Vol 2, Hemisphere Publishing Co., New York, 1989.

13. **Žukauskas, A.**, "Heat Transfer from Tubes in Crossflow," *Advances Heat Transfer*, Vol. 8, pp. 93-160, 1972
14. **Žukauskas, A.**, and **Ulinskas, R.**, "Banks of Plain and Finned Tubes," in *Heat Exchanger Design Handbook*, Vol. 2, Hemisphere Publishing Co., New York, 1984.
15. **Yang, R.J.**, **Lin, S.J.**, and **Chang, J.L.C.**, "Numerical Simulation of Flowpaths in the SSME Hot Gas Manifold," 5th SSME Computational Fluid Dynamics Workshop Meeting, Huntsville, Alabama, April, 1987.



# Report Documentation Page

1. Report No.		2. Government Accession No.		3. Recipient's Catalog No.	
4. Title and Subtitle  CFD MODELING OF TURBULENT FLOWS AROUND THE SSME MAIN INJECTOR ASSEMBLY USING POROSITY FORMULATION				5. Report Date  May, 1992	
				6. Performing Organization Code	
7. Author(s)  Gary C. Cheng Y. S. Chen Richard C. Farmer				8. Performing Organization Report No.	
				10. Work Unit No.	
9. Performing Organization Name and Address  SECA, Inc. 3313 Bob Wallace Avenue, Suite 202 Huntsville, AL 35805				11. Contract or Grant No.  NAS8-38871	
				13. Type of Report and Period Covered  Contractor - Final	
12. Sponsoring Agency Name and Address  George C. Marshall Space Flight Center Marshall Space Flight Center, AL 35812				14. Sponsoring Agency Code	
15. Supplementary Notes					
16. Abstract The hot gas turbulent flow distribution around the main injector assembly of the Space Shuttle Main Engine (SSME) and the LOX flow distribution through the LOX posts have impact combustion phenomenon inside the main combustion chamber. In order to design a CFD model to be an effective engineering analysis tool with good computational turn-around time (especially for 3-D flow problems) and still maintain good accuracy in describing the flow features, the concept of porosity was employed to describe the effects of blockage and drag forces due to the presence of the lox-posts in the turbulent flowfield around the main injector assembly of the SSME. A non-isotropic porosity model was developed and incorporated into the FDNS CFD code. Volume and surface porosity parameters, which are based on the configurations of local lox-post clustering, were introduced into the governing equations. Accuracy and robustness of the model was demonstrated through data comparisons with <u>some benchmark test data and with detailed benchmark CFD solutions</u> . Application of the model to the hot gas around the main injector assembly of the SSME was made, and the resulting flowfield was analyzed.					
17. Key Words (Suggested by Author(s))  SSME Powerhead, porosity model			18. Distribution Statement  unclassified - unlimited		
19. Security Classif. (of this report)  unclassified		20. Security Classif. (of this page)  unclassified		21. No. of pages  53	
				22. Price	